

Towards Autonomous Robotic Precision Harvesting

Edo Jelavic*

Dominic Jud

Pascal Egli

Marco Hutter

Abstract

This paper presents an integrated system for performing precision harvesting missions using a walking harvester. Our harvester performs a challenging task of autonomous navigation and tree grabbing in a confined, Global Positioning System (GPS) denied forest environment. Strategies for mapping, localization, planning, and control are proposed and integrated into a fully autonomous system. The mission starts with a human or a mobile robot mapping the area of interest using a custom-made sensor module. Subsequently, a human expert or a data-supported algorithm selects the trees for harvesting. The sensor module is then mounted on the machine and used for localization within the given map. A planning algorithm searches for both an approach pose and a path in a single path planning problem. We design a path following controller leveraging the walking harvester’s capabilities for negotiating rough terrain. Upon reaching the approach pose, the machine grabs a tree with a general-purpose gripper. This process repeats for all the trees selected by the operator (algorithm). Our system has been tested on a testing field with tree trunks and in a natural forest. To the best of our knowledge, this is the first time this level of autonomy has been shown on a full-size hydraulic machine operating in a realistic environment.

1 Introduction

Forests cover roughly 30% of the world’s land surface [United Nations Food and Agricultural Organization, 2018]. Forests provide the human population with raw materials, and they are a significant source of energy. Besides, forests provide a habitat for animal wildlife and contribute to the fight against climate change. Therefore, efficient forest management is of interest to all humankind.

The forestry industry has a share of 1.2% in the world’s Gross Domestic Product (GDP) and employs about 30-45 million people [Renner et al., 2008]. In some countries, forest industry products have a significant share in the total value of exported goods, e.g., Finland(18%), Latvia(16%) [Swedish Forest Agency, 2014]. Given the growing labor, shortage [Hawkinson, 2017], and classification of tree harvesting as a *3D* job (dirty, difficult, and dangerous), automation of forestry operations will be of high importance in the future.

1.1 Automation in Forestry

Mechanization in forestry has brought greater productivity; up to the point where the human operator has become the bottleneck in the whole process [Parker et al., 2016]. Since modern machines have many Degrees

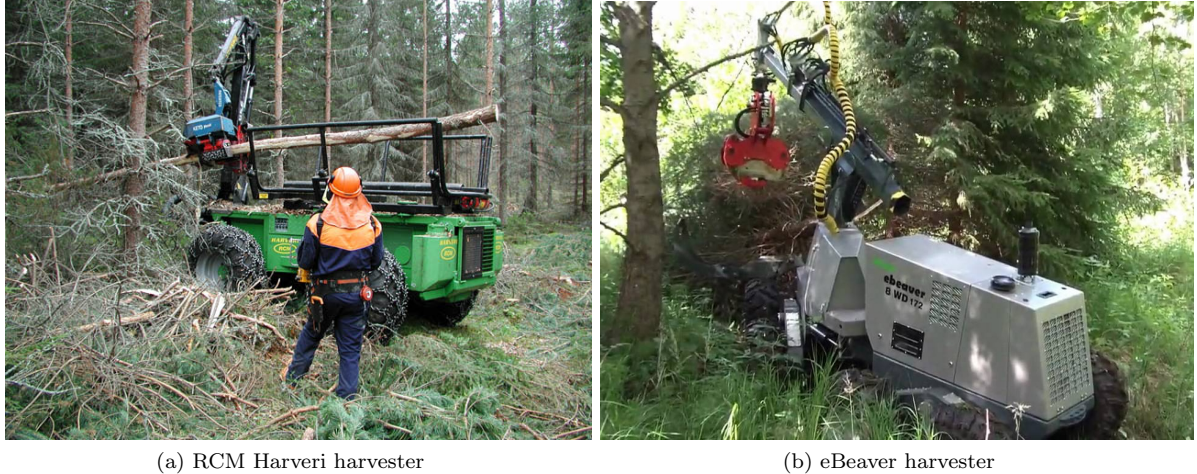
* All authors are with the Robotic Systems Lab, ETH Zurich, 8092 Zurich, Switzerland, email: edo.jelavic, dominic.jud, marco.hutter @mavt.ethz.ch, pascalarturo.egli@mavt.ethz.ch. Corresponding author: Edo Jelavic



(a) Komatsu-895 forwarder

(b) Komatsu-951 harvester

Figure 1: Different machines are typically used in modern forestry operations. They all have operator cabins to increase the comfort level in a possibly wet and muddy forest environment. Images were taken from [Komatsu Corporation, 2019]



(a) RCM Harveri harvester

(b) eBeaver harvester

Figure 2: Smaller harvesters that are typically used for thinning operations. They do not have a cabin for the operator and are remotely controlled within the operator's line of sight.

of Freedoms (DoFs), training good operators takes a long time, which presents a serious impediment to productivity increase. To mitigate the problem, researchers have tried to develop semi-autonomous modules for the crane operation in modern machines such as ones shown in Fig. 1a and Fig. 1b. Examples of such work can be found in [Westerberg, 2014, Ortiz Morales et al., 2014, Hyyti et al., 2018, Hellström et al., 2008].

Besides harvesting, a common task in forestry is thinning. Thinning is a process where we selectively remove some trees to make more space for others to grow [Forestry Focus, 2018]. Thinning requires negotiating tight spaces (as opposed to traditional clear-cutting) and can be done with smaller machines that are remotely controlled within the operator's line of sight. Two examples: Harveri and eBeaver, both shown in Fig. 2. Despite the lower cost and less damage to the forest ground than large harvesters, machines such as Harveri are not very popular since operators are reluctant to give up a cabin's comfort and safety.

1.2 Precision Forestry

Traditional forestry operations are still primarily based on fundamentals developed about 300 years ago [Von Carlowitz and von Rohr, 1732]. Nowadays, the trend is to move towards precision forestry. Instead of compartment-based management based on human experience and qualitative judgment, the forest's massive digital data enables much more granular and quantitative management. With the newest sensing technologies (e.g. Light Detection And Ranging (LIDAR)), precision forestry can even be done on the single tree level [Choudhry and O'Kelly, 2018], [Holopainen et al., 2014]. Compared to the traditional techniques, precision forestry diminishes the error in inventory estimates by 400 percent [Choudhry and O'Kelly, 2018]. Furthermore, there are other benefits such as granular fertilizing, fire monitoring, pest and disease monitoring that can increase yields and labor productivity up to 10 times [Silvere, 2017].

1.3 Scope

This article presents an approach for carrying out autonomous forestry missions, particularly harvesting and thinning (referred to as harvesting in other text). We primarily focus on executing an autonomous mission and all the aspects that executing such a task entails, namely mapping, localization, planning, control, and tool positioning. To this end, we develop a versatile sensor module for data collection and localization of the harvesting machine. We present our hardware platform, an automated Menzi Muck M545 harvester [Jud, 2018] equipped with custom sensors and actuators (see Fig. 3), and outline the technical approach used to carry out a harvesting mission planned by an expert (a human or a data-supported algorithm). Furthermore, we present experiments of a potential harvesting mission in the forest, and we state our findings and recommendations for tuning and system integration.

High-level decisions on which trees to cut and how to manage the forest inventory are beyond this article's scope. Nowadays, companies can create forest inventories and recommend future actions with aid from machine intelligence (e.g., [Silvere, 2017]), and our pipeline assumes using such a service. We focus on automating the workflow until the moment of cutting the tree. Cutting and debranching are not investigated since there are existing harvesting tools for this process.



Figure 3: Walking excavator navigating to a tree and performing a grab. Human is in the cabin for safety reasons.

This is the first field report of deploying large-scale machines for fully autonomous forestry missions to the best of our knowledge. Our approach enables operations under the forest canopy, which are significantly harder than clear-cutting since the machine has to drive between the trees where GPS signal may be unreliable. In summary, our work extends state of the art presented in Section 2 with the following contributions:

- Design of a portable sensor module with a sensor setup that enables mapping and localization. We test our sensor module in handheld operation, and we deploy it on a robotic platform.
- Development of a robust algorithm for converting raw point clouds into 2.5D elevation maps. The applicability of the algorithm is shown in a real forest and in several other environments. Our implementation is available as open-source¹.
- We develop an approach pose planning algorithm suited for tight spaces and both structured and unstructured environments. Algorithm evaluation on synthetic and maps produced from real data in a planning scenario includes large-scale harvesters.
- Development of a control approach for driving in rough terrain with a walking harvester. The algorithm performs path tracking and chassis stabilization at the same time.
- Both planning and path tracking algorithm implementations have been made publicly available for the community².
- We develop a method for tree detection based on LIDAR data. Our method is purely geometric based and operates directly on point clouds
- We integrate all system components into a functioning autonomous system. Experimental verification of the proposed pipeline is done on a full-size walking harvester in a realistic environment

2 Related Work

No autonomous system for thinning or harvesting missions has been presented in the literature so far. The harvester presented in [Rossmann et al., 2009] is the closest to our work in the sense that developed methods are showcased on a full-size machine. The authors develop a particle filter-based localization for forest environments; however, no attempt to automate other machine parts was made.

To acquire an overview about the forest and plan for harvesting, maps are typically first acquired by airborne surveying [Naesset, 1997], [Roßmann et al., 2009]. For mapping and localization, LIDAR sensors are a popular choice. GPS based localization can be inaccurate under a forest canopy, and vision-based sensors (cameras) can be sensitive to illumination changes in outdoor environments. For LIDARs, Iterative closest point (ICP) is a popular method for scan registration and has been used for mapping in forest surveying [Morita et al., 2018, Yue et al., 2018, Tsubouchi et al., 2014]. In [Babin et al., 2019], ICP is fused with GPS for mapping subarctic forests with sparse canopy. Another possibility is to use filtering with trees as landmarks. [Roßmann et al., 2009, Rossmann et al., 2010] build a map using an airborne laser sensor and localize a harvester in $SE(2)$ space using a particle filter. In [Miettinen et al., 2007], an Extended Kalman Filter (EKF) based Simultaneous Localization and Mapping (SLAM) is used on a skid steer robot to build a map and localize within it. The downside of relying on tree landmarks is that it can be susceptible to false positives. However, LIDAR mapping does not have to rely on landmarks. Thus, mapping algorithms such as [Hess et al., 2016, Zhang and Singh, 2014, Zhang and Singh, 2015] can potentially handle the most general classes of forests (sparse, dense, thick vegetation, etc.). Additionally, some mapping algorithms such as [Hess et al., 2016] allow for place recognition and have the advantage over ICP based mapping since they can correct the accumulated drift.

¹https://github.com/ANYbotics/grid_map/tree/master/grid_map_pcl

²https://github.com/leggedrobotics/se2_navigation

A harvester can be treated as a big mobile manipulator. Planning and control for mobile manipulators is a well-studied problem in robotics. One can either treat the robot in a whole-body fashion [Kim et al., 2019, Gifthaler et al., 2017, Gawel et al., 2019] or decouple the planning and control for the arm and the base [Carius et al., 2018, Schwarz et al., 2017]. The latter approach has often been used for forestry automation. Controlling the harvester’s (or forwarder’s) crane is an integral part of forestry operations. Examples can be found in [Lindroos et al., 2015, Westerberg, 2014, La Hera et al., 2009, Kalmari et al., 2014]. A major effort was put towards semi-automating the crane operation since coordinating many DoFs is one of the hardest tasks for a human operator. Most crane control algorithms are based on Inverse Kinematics (IK) or Inverse Dynamics (ID) [Siciliano et al., 2010]. Compared to classical robotic manipulators, the biggest difference is that harvester cranes were seldom designed with autonomous operations in mind. They often come without sensing capabilities which means they have to be retrofitted with sensors to estimate the end-effector position. Moreover, the sensors have to be robust to withstand operation outdoors—such retrofitting results in increased automation effort. An additional difficulty is that hydraulic actuators are harder to control than their electric motors counterparts (nonlinearities, valve overlap, less bandwidth). To minimize the automation effort, [Morales et al., 2011, Ortiz Morales et al., 2014] investigate possibilities for purely open-loop control.

Little has been done to develop a fully autonomous system for forest environment missions; the robotic community has mostly focused on urban environments. [Mikhaylov and Lositskii, 2018] shows a very simplistic architecture without any validation. In [Hellström et al., 2008] and [Georgsson et al., 2005], a GPS based tracking approach is presented and validated on a forwarder machine outside of a forest environment. [Tom-inaga et al., 2018] show experiments on an All Terrain Vehicle (ATV) without an arm in a small scale environment using GPS with Real-time Kinematic (RTK) correction. The authors use a global graph-based mission planner and a local state space sampling planner. A pure-pursuit algorithm is used for tracking. The proposed planning and control strategy cannot handle backward driving, limiting its ability to negotiate confined spaces. [Zhang et al., 2019] presents an integrated system for navigation in a forest. The authors present a planner and a path follower that run on a small skid-steer robot without an arm. They show results in a structured forest (a rubber tree farm) where trees form a grid. This is reflected in the path generation algorithm, which involves heuristics to exploit the environment’s structure and generates only straight-line paths.

3 Hardware

We introduce the robot used and we describe sensor module developed for the autonomous missions.

3.1 Platform

Our robotic platform is Hydraulic Excavator for Autonomous Purpose (HEAP). It is based on a Menzi Muck M545 multi-purpose walking machine often used for harvesting in challenging terrain. It is customized for teleoperation and fully autonomous operations. Besides forestry work HEAP, can be used for digging, landscaping and manipulation tasks as well (see [Jud et al., 2019], [Johns et al., 2020]). We use the terms HEAP and harvester interchangeably in further text. Our machine is fitted with custom hydraulic actuators with pressure sensors and a high-performance servo valve. The actuators allow for precise force and position control, thus enabling active chassis balancing and adaptation to the uneven ground (see [Hutter et al., 2016]).

Proprioceptive Sensing: Two SBG Ellipse2-A Inertial Measurement Unit (IMU)’s (one in the cabin and one in the chassis) gather the inertial data that are primarily used to determine the chassis’ roll and pitch angle. HEAP is equipped with a series of IMUs rigidly attached to each arm link. Measurements from these IMUs are fused together to estimate end-effector pose and joint angles in the machine frame. Note that, unlike in [Jud et al., 2019], we do not use externally mounted draw-wire encoders on the arm. This way, we avoid



(a) Front sensors on the cabin

(b) Localization sensor module in the back

Figure 4: **Left:** two LIDAR sensors mounted on top of the cabin and used for scanning the area in front of the machine. They are primarily used for tree detection. **Right:** The localization module introduced in Sec. 3.2 mounted in the back of the machine.

a potential entanglement of draw wires with tree branches.

Exteroceptive Sensing: Two Velodyne Puck VLP-16 LIDAR's are used for tree detection. It is important to note that one of the Pucks is rotated by 90° around the rolling axis (see Figure 4a) in order to get a better resolution when mapping the area in front of the machine. A sensor module (see Sec. 3.2) is mounted on the back of the machine, as shown in Figure 4b.

The planning, control, and tree detection software stack runs on one computer (Intel i7-5820K, 6x3.60GHz, Ubuntu 18.04) installed in the cabin. The control loops work at 100 Hz and are triggered by the Controller Area Network (CAN) driver. All the algorithms presented are implemented using C++.

3.2 Sensor Module

We develop a sensor module for mapping and localization as displayed in Figure 5. The module can be used in the first step by a human to map the area of interest (see Fig. 6a). In a second step, the system can be mounted on HEAP (Fig. 4b) to localize the machine in the previously built map without GPS information.

We design the sensor module to be lightweight such that handheld operation is possible. It has an integrated computer such that mission data can be collected and saved without an external laptop. Besides, one can run the SLAM directly on the module in real-time. The module has a LIDAR, an IMU, and two visual sensors. LIDAR is used as a primary sensing modality with aid from visual and inertial sensors. This way, the motion distortion in the point cloud can be corrected. Lastly, all sensors installed on the module are time-synchronized. Time synchronization is essential for state estimation and mapping algorithms to function correctly.

The sensor module in operation is shown in Fig. 6a and sensor components in Fig. 5a. We use an Ouster OS-1 LIDAR with 64 channels, an Intel Realsense T265 tracking camera, and a FLIR camera model BFS-

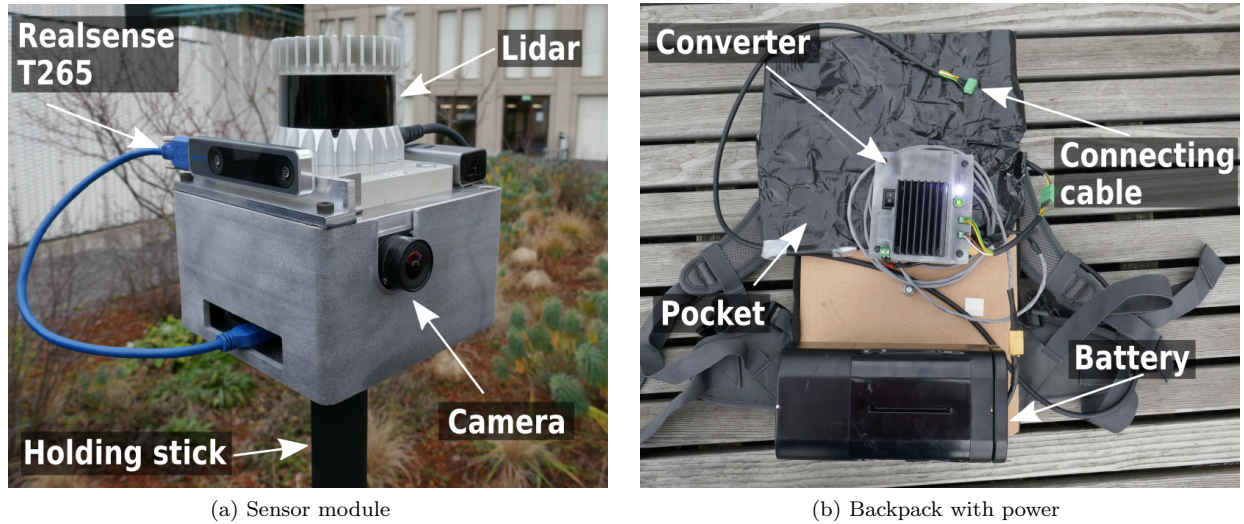


Figure 5: **Left:** Head of the sensor module. The Central Processing Unit (CPU) and the IMU are inside the grey box. **Right:** Power supply for the sensor module mounted on the backpack.

U3-04S2M-CS. Inside the grey box in Fig. 5a, one can find a computing unit (Intel NUC with i7-8650U processor) and an IMU (Xsens MTI-100). We implemented two complementary solutions for Visual Inertial Odometry (VIO): FLIR camera synced with IMU and the Intel Realsense T265 tracking camera. The FLIR camera has an excellent low light performance, while the T265 has almost 180° Field of View (FOV). Hence, one can choose the VIO sensor used depending on the application. The sensor module can be mounted on a stick shown in Figure 5a. In this way, a human can walk around with the module and point it to the places of interest to map it in sufficient detail. The sensor module is powered from the backpack (shown in Fig. 5b), equipped with a 36 V battery. We choose to use a 300 W h e-bike lithium-ion battery (BiX Power BX3632H) with an integrated battery management system. All smaller sensors like cameras and the IMU are powered through Universal Serial Bus (USB).

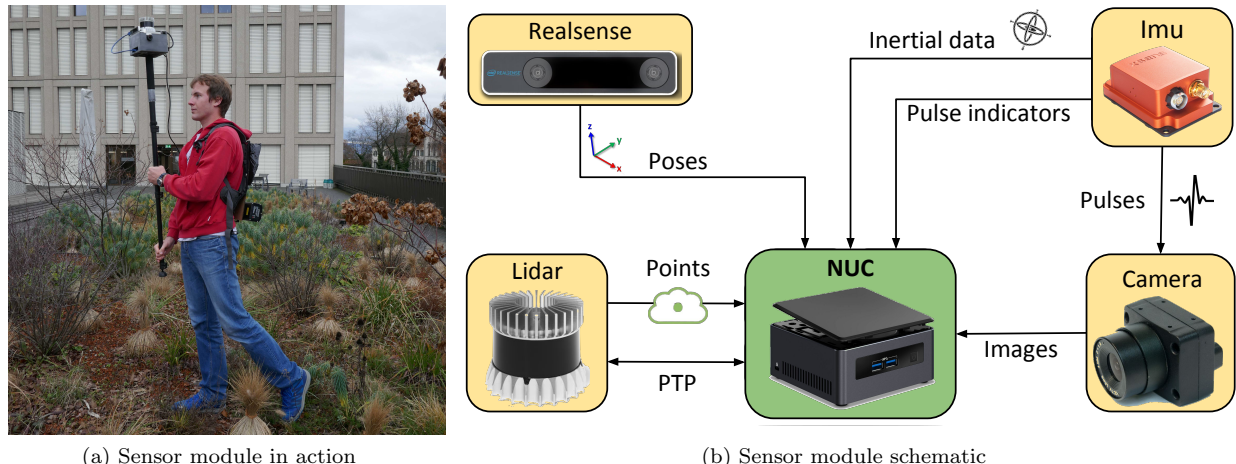


Figure 6: **Right:** Human operator mapping an area of interest. **Left:** Schematic of the sensor module. It is composed of a camera, tracking camera (realsense), LIDAR and an IMU.

The schematic of the sensor module is shown in Fig. 6b. The Intel Realsense camera provides software-

synchronized VIO at a frequency of 200 Hz. The FLIR camera and the IMU are synced using customized software. However, in this work, we rely on VIO from the T265 tracking camera. The LIDAR is connected directly to the computer, and it is configured to use Precision Time Protocol (PTP) for time synchronization [Eidson, 2006]. We modify the LIDAR’s driver to send the packets as soon as they are received instead of batching them until the scan is completed. This way, the motion distortion is mitigated. We use the TICsync package [Harrison and Newman, 2011] to synchronize the IMU with computer’s clock. TICsync estimates the bias and the drift between the IMU’s internal clock and the computer’s clock to recover the exact time when the measurement happened. To increase the robustness, it is beneficial to assign the real-time priority to the IMU driver (minimizes the timestamp jitter).

4 Approach Overview

Fig. 7 presents an overview of the autonomous harvesting system and serves as a visual outline for the chapters in this paper. We briefly describe each subsystem and give a more detailed description in their respective chapters.

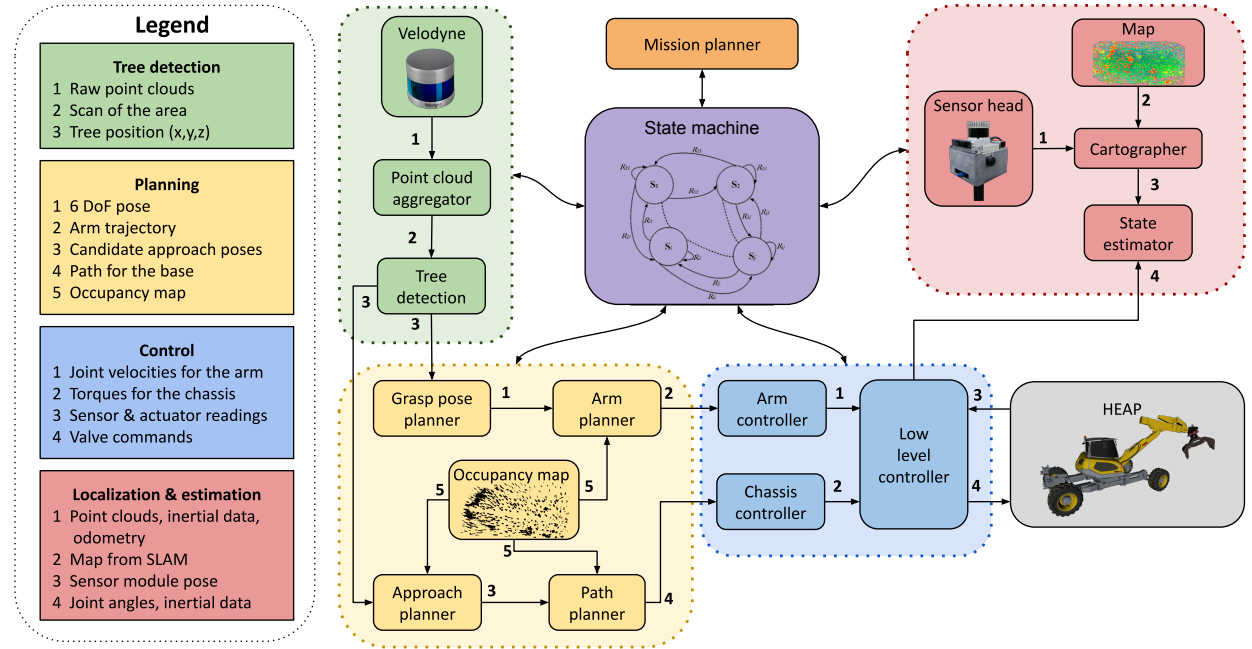


Figure 7: Overview of the system architecture deployed on HEAP. Components belonging to the same subsystem are shown in the same color. Different subsystems are shown in different colors. Arrows depict communication channels in the system, with some communication lines omitted for the sake of brevity.

Mapping and Localization: We use a LIDAR based SLAM together with visual and inertial measurements to correct for scan distortion. The map is built by processing the data offline. At mission time, scans are registered against the existing map to compute the sensor module’s pose.

Tree Detection: The LIDAR sensors mounted on the top of the cabin (see Figure 4a) deliver point clouds at 20 Hz. An intermediate node aggregates them and passes them to the tree detection module. Detection is done purely based on geometric features. The tree detection module forwards the detected tree’s coordinates to the grasp pose planner and the approach pose planner.

Control: The control subsystem is split into two parts. The arm controller ensures trajectory tracking by sending velocity commands to the arm joints (IK controller). The base controller ensures path tracking, and

Table 1: Order of operations and subsystems involved to grab a single tree

Task order	Task Description	Subsystems responsible
1	Get the next tree position.	Mission planner
2	Plan an approach pose and a path. If it fails, go to step 1.	Planning
3	Drive the machine to the approach pose found in step 2. In case tracking fails, go to step 2	Control
4	Retract the arm (in case it is not already retracted)	Planning, Control
5	Scan the area around the expected tree location.	Control
6	Run tree detection algorithm and plan a grasp pose	Tree detection, Planning
7	Plan and track an arm trajectory to reach the grasp pose	Planning, Control
8	Plan and track arm trajectory back to default position (arm retracted all the way).	Planning, Control
9	Go to step 1.	State Machine

it regulates contact forces such that the base stays upright when driving over uneven terrain. The low-level controller transcribes higher level references (velocity, torque, positions) to the valve commands.

Arm and Base Motion Planning: The planning stack comprises three planners. The base planner plans a path and an approach pose for the base of the harvester. The grasp pose planner computes a gripper pose in 3D space that encompasses the tree trunk. Finally, the arm planner produces a collision-free sequence of waypoints to move the gripper into the desired pose.

Mission Planning: This module determines which tree to grab next, and it sends the target position to the state machine, which then sends it to the approach pose planner.

State Estimation: The state estimator uses the sensor module pose and proprioceptive measurements (IMU, joint angles) to compute the complete state of the system (6 DoF base pose + joint angles).

State Machine: The state machine coordinates the execution of different tasks. It works on a handshaking principle where the state machine sends a request to a subsystem, and the subsystem responds with an acknowledgment once the task requested has been completed. Tasks that the state machine can request and the order of operations to grab a single tree are shown in Tab. 1.

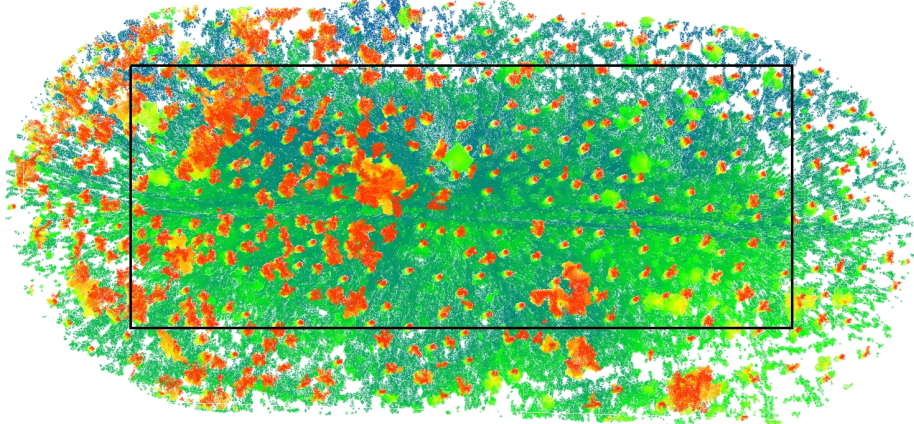
5 Mapping and Localization

Precision forestry requires precise and consistent 3D geometric information about the forest. This data can be collected by a harvester itself, a smaller Unmanned Ground Vehicle (UGV) or by a human carrying the sensors. The collected information can then be used for mission planning and forest inventory management. Moreover, the map serves as a reference for the harvester to localize. To retain flexibility, we would like to make no assumptions on the surroundings and allow the harvester to work in different types of forests (e.g., sparse, with vegetation, non-flat). Therefore we avoid using tree stems as landmarks (e.g., [Roßmann et al., 2009]) since they can be hard to detect (vegetation) or they may be scarce (e.g., a glade inside the forest).

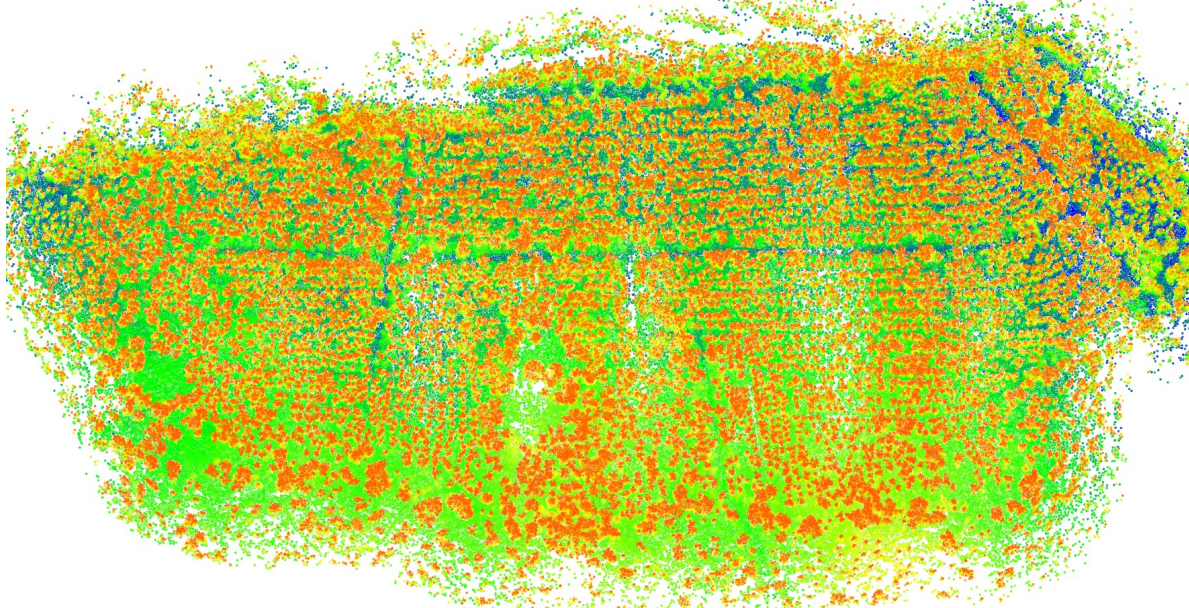
We selected Google Cartographer [Hess et al., 2016] as the backbone of our mapping and localization pipeline. Cartographer is a grid-based SLAM approach that uses the scan to sub-map matching for loop closure detection and discards unlikely matches using the branch and bound method. At mission time, localization can be achieved simply by scan to sub-map matching.

5.1 Mapping

Examples of maps generated with Cartographer is shown in Fig. 8.



(a) Testing forest patch



(b) Large forest area

Figure 8: Bird view of forest maps. Both maps are represented as point clouds. **Top:** Small forest patch where we conducted the experiments. Approximate size 140 m x 60 m. The area encircled with a black rectangle was converted to an elevation map (Fig. 9). **Bottom:** Map of a larger forest area (top view), where the data has been collected in multiple tours, concatenated and the processed with Cartographer [Silvere, 2017]. Approximate size: 340 m x 170 m

Map in Fig. 8a shows a point cloud of a forest viewed from above. Blue and green colors correspond to a lower elevation (ground), whereas yellow and red colors correspond to a higher elevation (vertical structures like tree trunks and canopy). The map is about 140 m long and 60 m wide, and it shows a part of the forest where we conducted the experiments with HEAP. Another, larger map (340 m x 170 m) is shown in 8b; the size of this map shows that Cartographer can map areas sufficiently large for an autonomous harvesting mission. Both maps have been processed offline and bundle adjusted. Once the map and trajectory have

been optimized, we can compute an elevation map. Below we detail the conversion of the point cloud into an elevation map used by the planner.

A grid map data structure [Fankhauser and Hutter, 2016] is used to store the elevation map. From the raw point cloud in Fig. 8a, our algorithm builds a 2.5D elevation map of the area shown in Fig. 9. Conceptually, the algorithm is similar to the one used in [Fankhauser et al., 2018]. In contrast to [Fankhauser et al., 2018], our algorithm can handle multiple elevations in the cell, i.e., multiple points with the same (x, y) coordinates and different z coordinates. Thus, it can filter out vegetation and clutter and recover true ground elevation more robustly. We successfully used the point cloud to elevation map conversion algorithm in both planar and non-planar environments. Implementation is available as an open-source package³.

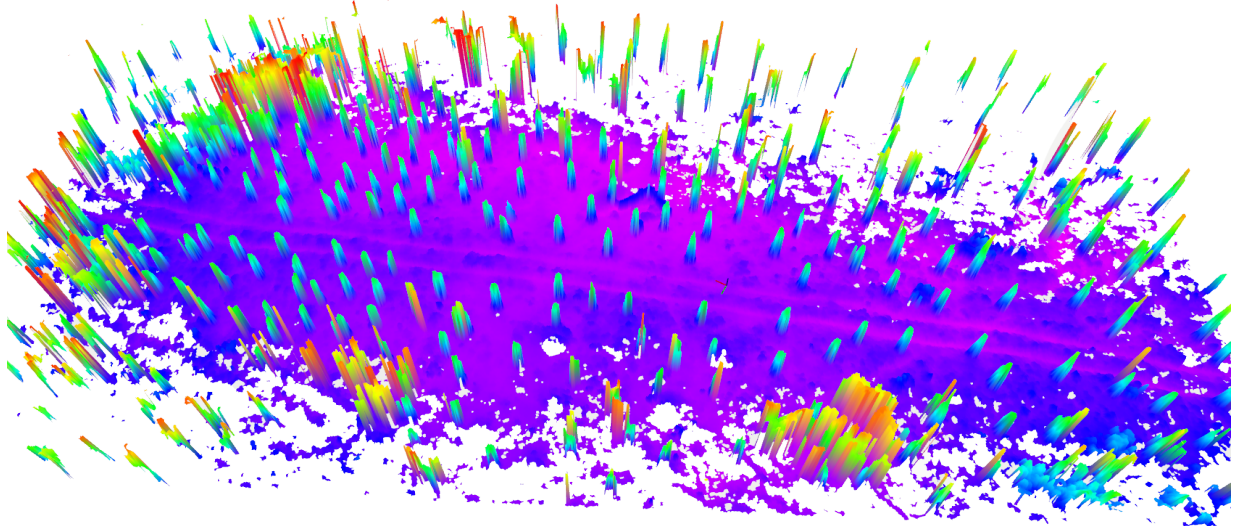


Figure 9: Elevation map of a forest patch encircled black in Fig. 8a. The resulting grid map size is 1419 by 1318 cells with a resolution of 10 cm. Note how tree trunks are clearly visible in the elevation map.

The point cloud to elevation map conversion algorithm starts by removing the outliers and downsampling the input point cloud (implementation based on [Rusu and Cousins, 2011]). The main loop is paralleled to speed up computation. For each cell in the grid map, we pre-compute all the points contained within that cell (this enables lookup in $O(1)$ time), thus vastly speeding up the algorithm. Each cell is a rectangle in x, y coordinates. Once we have fetched the points inside the grid map cell, Euclidean clusters are computed. Subsequently, we calculate the centroid of each cluster. Finally, the centroid with the smallest z coordinate is deemed to be the ground elevation. Illustration of the process shown in Fig. 10.

In Fig. 10, grid map cells are extended in the z direction and form columns 1, 2, and 3. Column 1 has one cluster which contains only the ground points (shown in light green), and the algorithm correctly extracts the ground height. In column 3, the algorithm extracts at least two clusters. The lower cluster is the ground (light green color), while branches and leaves form the upper cluster (dark green). Clusters are disjoint, and the algorithm correctly recovers the ground elevation as a mean value of the lower cluster. Column 2 contains one large cluster composed of both ground and the tree. In this case, we cannot recover ground information since the resolution of the map is too coarse; the height of the tree trunk determines the height. In this work, we use the resolution of 10 cm for the grid.

Qualitative runtimes of our algorithm are shown in Tab. 2. The foreseen use case is to run the algorithm once offline to construct a global elevation map that can be used for planning. The times shown in Table

³https://github.com/ANYbotics/grid_map/tree/master/grid_map_pcl

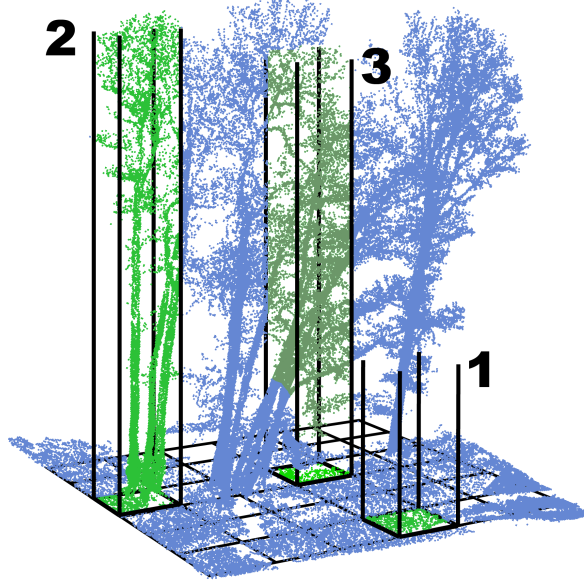


Figure 10: Generating a grid map from a raw point cloud. The grid is shown with black lines, and the input point cloud is shown in blue color. Clusters of points that the conversion algorithm might extract are shown in green. Note that image is not drawn to scale.

2 were obtained on an Intel Xeon E3-1535M (2.9 GHz). The algorithm is not limited to application in forests only but also generalizes to non-forest environments (see https://github.com/ANYbotics/grid_map/tree/master/grid_map_pcl)

Table 2: Qualitative runtimes of the point cloud to elevation map conversion.

Point cloud size	less than 10 million points	40-60 million points	100 - 140 million points
Algorithm runtime	1-2 minutes	5-15 minutes	30-60 min

5.2 Localization

Apart from mapping, the sensor module from Sec. 3.2 is used to localize HEAP within the map. The localization pipeline consists of components encircled in red color in Figure 7. The sensor module is mounted on the excavator (as shown in Fig. 4b). The sensor module’s clock is synchronized to the harvester’s computer clock using Network Time Protocol (NTP). PTP and NTP run on different networks. We forward all the measurements to the main computer running Google Cartographer in the localization mode (see [Hess, 2017]).

Cartographer gives a pose estimate of the sensor module in the map frame used to compute the excavator’s entire state. Extrinsic calibration of the sensor module mounted on HEAP is obtained from Computer Aided Design (CAD) model and manual measurement. The setup with the sensor module mounted in the back resulted in end-effector position accuracy (coupled errors from sensor module localization and robot kinematics) of about 30 cm. For evaluation, we have asked the harvester to grab the same tree blindly multiple times. Such a level of accuracy may not be enough for high precision harvesting, and we mitigate the problem by detecting the grabbing target in a locally built map (see Sec. 6).

6 Tree Detection

The tree detection subsystem's responsibility is to detect a tree trunk and compute its position. A schematic of the subsystem with some intermediate processing steps is shown in Fig. 11. Once HEAP is positioned close to a tree, the state machine initiates a scanning maneuver to create a map of the scene in the local frame. Tree detection in the local frame is less affected by inaccuracies in the global localization system. It is worth noting that the tree detector also works on global maps and can be used to aid mission planning; this is discussed in Sec. 9.3.1.

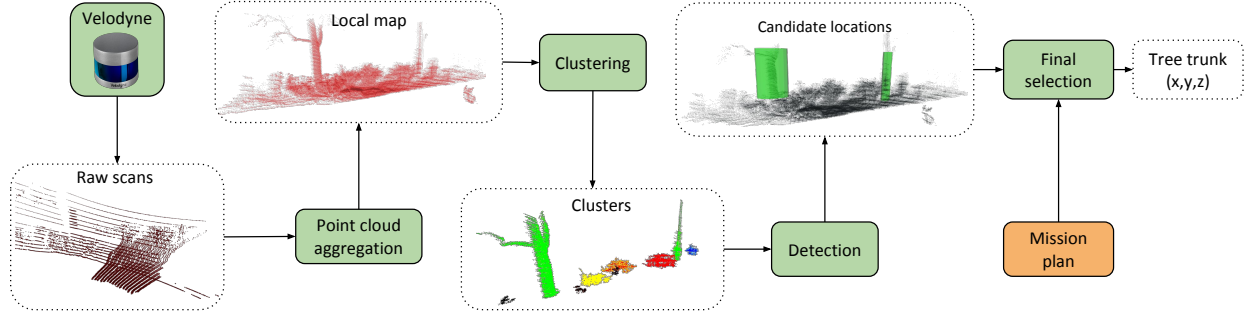


Figure 11: Flowchart of the tree detection subsystem procedure.

Tree detection starts with a scanning maneuver by rotating the cabin while the chassis is kept steady. The cabin is initially pointing in the direction where the harvester expects the target tree to be (known from the mission planner). The two LIDAR's mounted on the front of the machine (see Fig. 4a) stream the point clouds at 20 Hz. A receiver node stitches them together into a local map. The relative transformation between subsequent scans is recovered from the chassis's roll and pitch angle together with the cabin joint angle measurement. An example of a local map is shown in Figure 12a. The area scanned in Fig. 12a is somewhat larger than necessary to visualize steps in the tree detection algorithm better. We move the cabin $\pm 30^\circ$ to scan the area and build a local map during the deployment. This corresponds to double the horizontal FOV of the tilted Velodyne LIDAR (see Fig. 4a) such that a dense local map can be built.

The raw scans from LIDARs are transformed into the cabin frame and cropped to speed up the subsequent steps. Once cropped, the scans are transformed into a gravity-aligned frame where they are concatenated. Point cloud assembled from cropped scans cloud is shown in black in Fig. 12b (black). The assembled cloud is then gravity aligned and cropped again to filter out the ground plane and the tree crown (shown in red color, Fig. 12b). The red point cloud is sent to the tree detection module, which selects all prominent trees in the scan as shown in Fig. 12d.

The tree detection algorithm first computes Euclidean clusters in the input point cloud (shown in Fig. 12c). Euclidean clusters are searched using the algorithm from [Rusu, 2010]. We discard the clusters with too few points. Since most trees grow vertically, a point cloud of a tree trunk should have a majority of the points spread out along the z axis. Hence, Principal Component Analysis (PCA) is performed on each cluster, and we only keep clusters with a significant principal component along the z axis. Note that we can exploit the verticality assumption since our point cloud is gravity-aligned. The gravity alignment score ($\in [0, 1]$) is defined as the dot product of the largest principal component with a $[0 \ 0 \ 1]^T$ vector. Lastly, we check for the minimum height of the tree. The final detection result is shown in Fig. 12d. Sizes of bounding ellipsoids are computed based on principal components' eigenvalues in x and y direction. The final tree location is the ellipsoid's center. In the case of multiple tree detection (such as in Fig. 12d), the algorithm extracts coordinates of the tree closest to the expected tree position (from the mission planner).

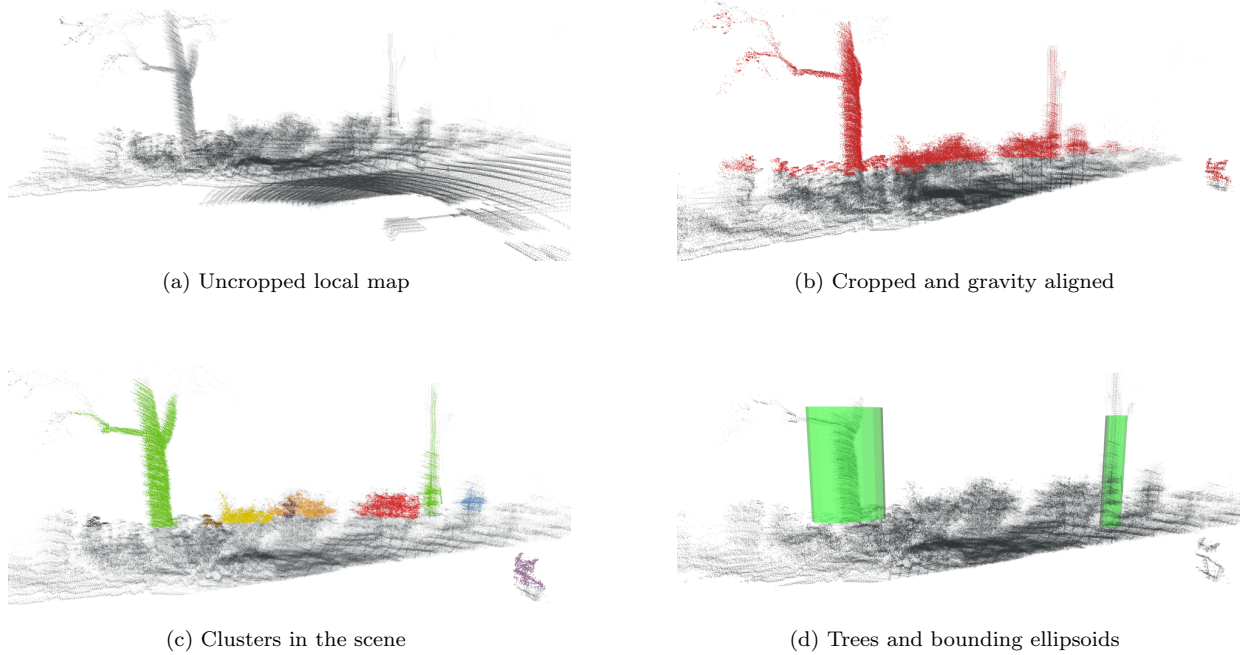


Figure 12: Intermediate results in the tree detection pipeline. **Top Left:** Scan of the area, without any cropping. One can observe the large ground plane in the point cloud. **Top Right:** Cropped point cloud after first and second cropping (red color). **Bottom Left:** Clusters in the scene. Each of these clusters is considered by the tree detection module. **Bottom Right:** Final tree detection with the resulting bounding ellipsoids.

7 Control

In this work, chassis control is responsible for locomotion and arm control for tree grabbing (harvesting). The respective control subsystems (shown in blue, Fig. 7) are described in more detail in this section.

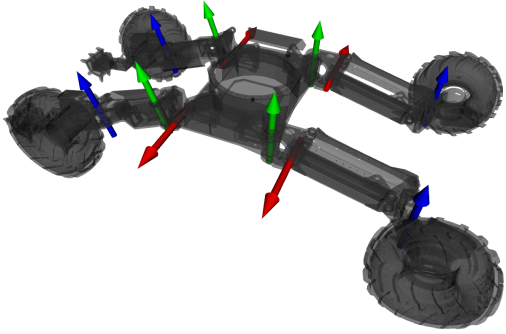
7.1 Chassis Control

HEAP has four legs with wheels allowing it to drive and adapt to the terrain (see Fig. 13.) Thereby, the goal is to optimally distribute the four wheels’ load to ensure traction and minimize terrain damage.

Terrain adaptation controller (also named Hip Balancing Controller (HBC)) is based on a virtual model control principle where the controller computes a net force/torque on the chassis to achieve the desired orientation (roll, pitch) and height. An optimal contact force distribution is computed from the net force/torque for all the legs. Contact force tracking is achieved via force tracking on the hydraulic actuator level. For more details, refer to [Hutter et al., 2016]. The described chassis controller can keep the base leveled while overcoming large irregularities in the terrain without getting stuck. Terrain adaptation is achieved using proprioceptive measurements only (joint sensing, IMU). We have extensively tested HBC performance in our previous work ([Hutter et al., 2015], [Hutter et al., 2016]). A video showing the machine overcoming challenging terrain can be found online⁴.

For path tracking, we use a pure pursuit controller similar to the one outlined in [Kuwata et al., 2008]. The pure pursuit controller calculates the turning radius (denoted with R) required to bring the machine on the

⁴https://youtu.be/5_Eq8CxKkvM



(a) Chassis schematic



(b) Chassis in action

Figure 13: **Left:** Illustration of the HEAP’s chassis. The cabin and the arm are not shown for the sake of clarity. Steering joints axes are shown with blue arrows, flexion joint axes with red, and abduction joint axes with green color arrows. The path following controller actuates the steering joints while the HBC actuates the flexion joints. Abductions joints are not used. **Right:** Chassis control system overcoming a stump during the deployment.

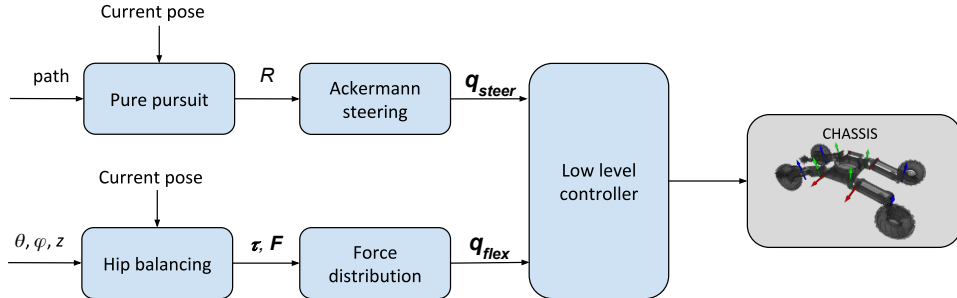


Figure 14: System diagram of the chassis control module deployed on HEAP.

path computed by the planner. The Ackermann steering module then calculates steering joint angles for each leg. Steering angles are computed such that all four wheels point to the same center of rotation with the radius R . The computation is implemented as a nonlinear optimization that satisfies all the kinematic limits and minimizes the required actuation.

The HBC and the pure pursuit controller are combined to locomote the harvester, as shown in Fig. 14. Both controllers close the feedback loop over position: HBC regulates the roll, pitch, and height, whereas pure pursuit ensures that x , y , and yaw are tracked correctly. The Ackermann steering module computes position reference for the steering joints (q_{steer} in Fig. 14), while the force distribution module computes joint torques assuming quasi-static conditions (q_{flex}). The low-level controller translates the joint quantities (torques, positions) into the valve commands. In Fig. 13b, the proposed controller is driving over a stump. Note how the controller retracts the left hind leg to maximize the traction. In parallel, the pure pursuit controller controls the driving direction.

7.2 Arm Control

Reaching the end-effector target position determined from the tree detection module is achieved using an IK controller (see [Siciliano et al., 2010]). The arm controller implementation is based on the Hierarchical Optimization (HO) approach (see [Bellicoso et al., 2016]). Besides tracking, HO computes joint velocities, enforces kinematic limits, and ensures that all flow constraints for hydraulic actuators are satisfied. Opening

and closing the gripper is controlled directly by the state machine.

8 Planning

In this section we describe the mission planner and the motion planning stack in more detail. The motion planning stack is divided into three components shown in Fig. 7: base planner, grasp pose planner and the arm planner.

8.1 Mission planner

To conduct the experiments, we design a mission planner which determines which tree to grab next. Before the mission, a human manually selects the trees to be cut using Graphical User Interface (GUI) shown in Figure 15, thus mimicking an algorithm for tree inventory management. When clicked on, a tree gets added to the tree list for harvesting with position coordinates extracted in the map frame. The mission planner passes the tree coordinates to the state machine in the same order as they were selected.

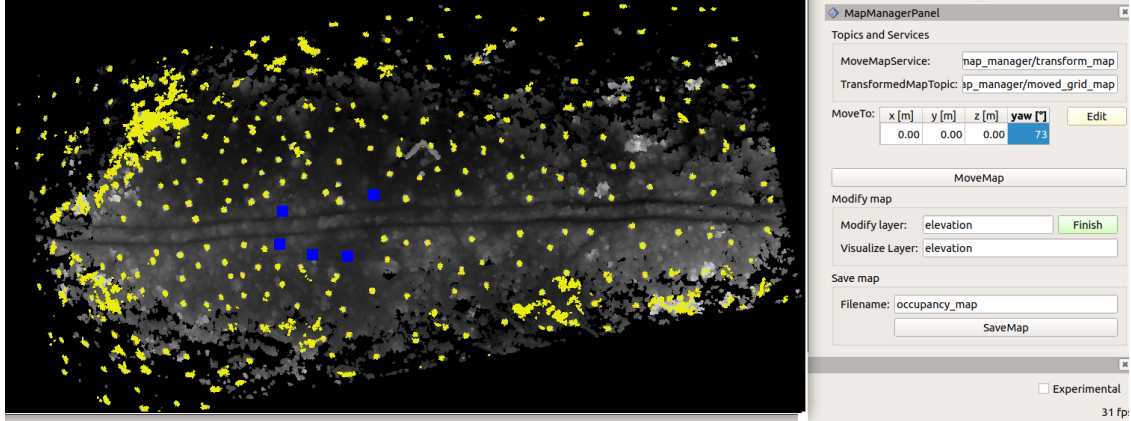


Figure 15: GUI used for mission planning. An elevation map is shown in black and white, white corresponding to a higher elevation. Tree trunks and parts of the canopy are colored in yellow. In this example, a total of five trees (marked with blue squares) are selected to be cut.

8.2 Base Pose Planning

We do not make any assumptions on the terrain properties; thus, our planner accounts for irregular terrain. Path planning in rough terrain is a complex problem, and in general, it has not been solved yet. In this work, we split it into two more manageable subproblems: planning in $SE(2)$ (instead of $SE(3)$) and traversability estimation.

8.2.1 Traversability Estimation

Traversability estimation has been previously studied, and different approaches for various sensing modalities exist. In this work, we use purely geometric traversability estimation, which can be directly applied to elevation maps without any additional processing. We follow the approach presented in [Wermelinger et al., 2016] that evaluates three criteria: terrain slope, roughness, and step height for local terrain patches (0.3 m radius). The final result is a weighted sum of all three components. We chose to mainly rely on step criterion (80 %) since the chassis control system introduced in Sec. 7.1 can overcome slopes and drive over

rough terrain. The remaining 20 % was assigned to the slope criterion to prevent the harvester from driving on very steep slopes, which could result in slipping.

Fig. 16a shows the traversability map; incorrectly classified areas (classified untraversable while it is traversable) are encircled red. Thick vegetation that occludes the ground from the LIDAR sensor during the mapping phase is the main culprit for false negatives. Since the overall misclassified area is small, a human can manually correct the errors. We used the GUI from Fig. 15 and the correction lasted about 2 minutes. Fig. 16b shows the corrected traversability map; note how the algorithm automatically classifies tree trunks as untraversable. Presented traversability estimation has an upside that is easy to implement; there is no need for elevation map processing or segmenting out the tree trunks explicitly. Fully automating the proposed pipeline would require additional work to eliminate the correction step and be implemented in future work.

The traversability map (see Fig. 16b) is converted into an occupancy map. Any traversability value smaller than 0.5 is deemed an obstacle, and higher values are regarded as free space. Motion planners use the occupancy map.

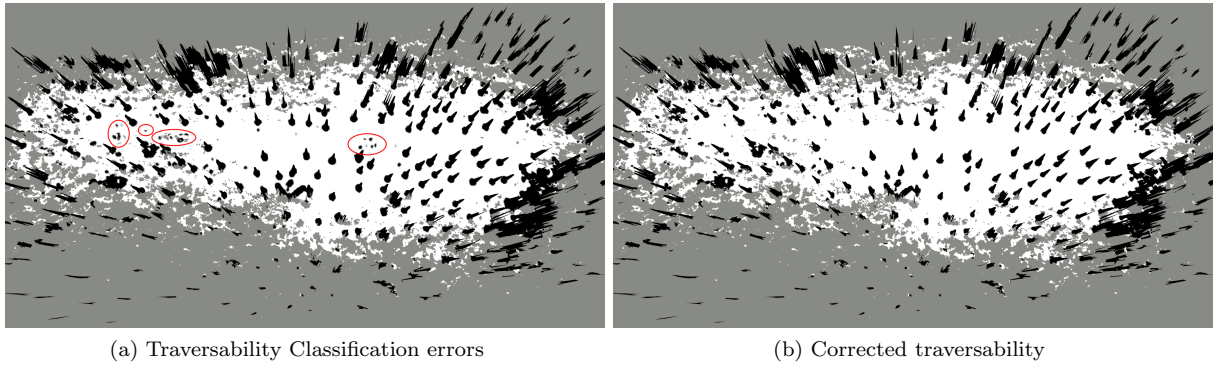


Figure 16: Traversability maps computed by our approach shown against gray background. White areas represent fully traversable terrain, whereas black areas represent terrain that is not traversable. **Left:** Red areas have been incorrectly classified as untraversable by the algorithm (false negatives). **Right:** Traversability map after applying the correction.

8.2.2 Path and Approach Pose Planning

The planning subsystem (shown in yellow color in Fig. 7) gets a tree position from the mission planner. The tree position is an approximate target location for the end-effector. The harvester should not reach the tree position itself because then it would be in a collision. To this end, we develop an algorithm for joint path and approach pose planning. We evaluate the algorithm in both simulations and natural environments.

Existing planning algorithms typically plan from starting pose to the goal pose. However, in our case, we do not know the goal pose (only approximate end-effector position in x and y). Hence, the proposed planning algorithm is split into two stages: first, the planner generates candidate poses and checks for their feasibility. Secondly, the planner tries to compute a path to any of the feasible candidates. Thus the approach pose planning is reduced to a common path planning problem, and we leverage a Rapidly-exploring Random Tree (RRT)* algorithm for a joint path and approach pose computation. Our implementation uses Open Motion Planning Library (OMPL), [Sucan et al., 2012].

The approach pose generating subroutine is shown in Alg. 1. It starts by getting a target/tree location $\mathbf{x}_T \in \mathbb{R}^2$ (line 1), and computing a set of approach poses around it (lines 12 - 22). We compute $M \times N$ approach positions in polar coordinates around \mathbf{x}_T by pairing M different distances to the tree with N

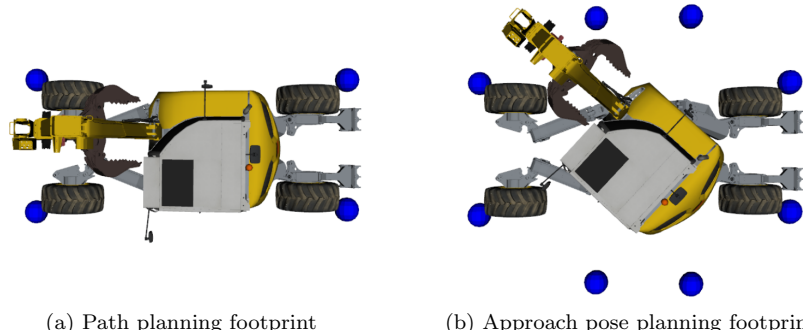


Figure 17: Top view of HEAP with the arm retracted with the footprint vertices shown in blue. Note: not drawn to scale. **Left:** Footprint used for path planning (see Alg. 2). **Right:** Footprint used for the approach pose generation (see Alg. 1) is wider in the middle, thus allowing for cabin turning.

uniformly distributed polar angles. Lastly, the approach positions are paired with K yaw angles (lines 19-21) to generate a total of $N \times M \times K$ candidate approach poses in $SE(2)$. To be a valid candidate, an approach pose must be collision-free (lines 5-6), the harvester’s arm must be able to reach the target (lines 7-8), and all heuristics must be satisfied (lines 9-10).

Algorithm 1 Candidate approach pose generator

```

1:  $x_T, y_T \leftarrow \text{GETNEXTTARGETLOCATION}()$ 
2: procedure COMPUTECANDIDATEAPPROACHPOSES( $x_T, y_T$ )
3:    $candidateApproachPoses \leftarrow \text{GETAPPROACHPOSESAROUNDTARGET}(x_T, y_T)$ 
4:   for each  $pose$  in  $candidateApproachPoses$  do
5:     if  $\text{ISINCOLLISION}(pose)$  then
6:        $candidateApproachPoses.\text{DELETE}(pose)$ 
7:     if  $\neg\text{ISTARGETREACHABLEFROM}(pose)$  then
8:        $candidateApproachPoses.\text{DELETE}(pose)$ 
9:     if  $\neg\text{ISHEURISTICVALID}(pose)$  then ▷ Optional
10:       $candidateApproachPoses.\text{DELETE}(pose)$ 
11:   return  $candidateApproachPoses$ 
12: procedure GETAPPROACHPOSESAROUNDTARGET( $x_T, y_T$ )
13:    $distances \leftarrow \{d_1, d_2, \dots, d_M\}$ 
14:    $polarAngles \leftarrow \{\phi_1, \phi_2, \dots, \phi_N\}$ 
15:    $headings \leftarrow \{\psi_1, \psi_2, \dots, \psi_K\}$ 
16:    $approachPoses \leftarrow \emptyset$ 
17:   for each  $d_i$  in  $distances$  do
18:     for each  $\phi_i$  in  $polarAngles$  do
19:        $(x_i, y_i) \leftarrow (x_T + d \cos(\phi_i), y_T + d \sin(\phi_i))$ 
20:       for each  $\psi_i$  in  $headings$  do
21:          $approachPoses.\text{ADD}([x_i, y_i, \psi_i])$ 
22:   return  $approachPoses$ 

```

The blue points shown in Fig. 17 represent the harvester’s collision footprint. The harvester is in a collision if there is an obstacle inside the blue points convex hull. Collision checks inside the Alg. 1 use the footprint shown in Fig. 17b. Note how the hull is wider in the middle to allow for cabin turns. The real-world map is abstracted away from the planner, and it only sees the obstacles computed by the traversability estimation step. Such a simplification is warranted by using a control system able to overcome slopes and rough terrain.

The target being reachable from an approach pose means that the harvester can safely extend the arm to

reach the goal position (see Alg. 1, line 7). We check whether there is a collision-free line of sight from the base to the target goal. Because of HEAP’s kinematic structure, the arm always stays within a slab in the $x - z$ plane (in the cabin frame). Hence, we require no obstacles inside the slab spanned by the target tree position and the base position. Therefore, there is no need for more complicated algorithms that are popular in mobile manipulation literature (e.g., [Zucker et al., 2013]). An example of the approach pose generation in a forest environment is shown in Fig. 18.

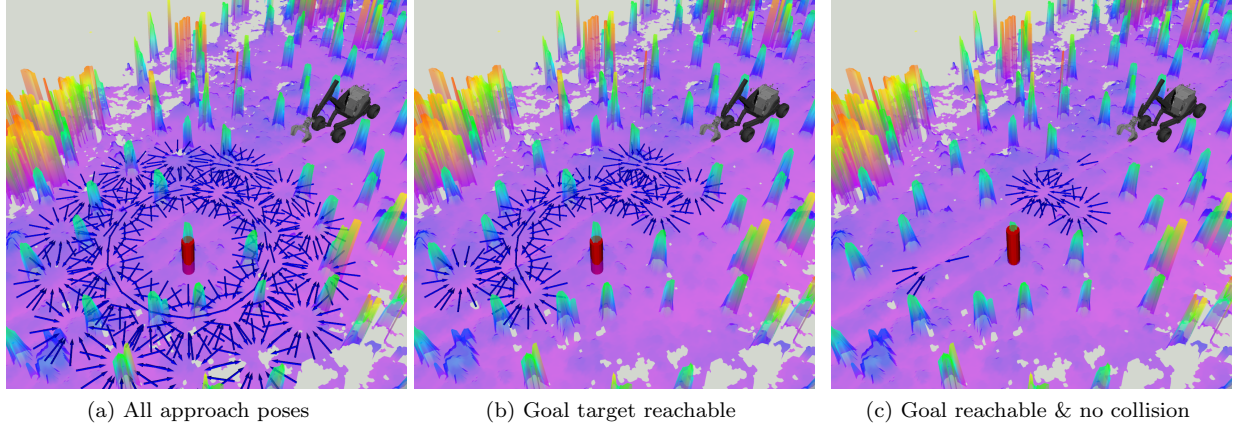


Figure 18: Approach pose generation in the forest environment. The elevation map with the target tree (red cylinder) and candidate approach poses are shown with blue arrows. Fewer approach poses are generated for the sake of clarity. **Left:** In total, 450 goal approach poses are generated. **Middle:** The arm can extend and grab the target tree from 195 poses. **Right:** From 27 approach poses, one can grab the target tree, and the machine is not in collision.

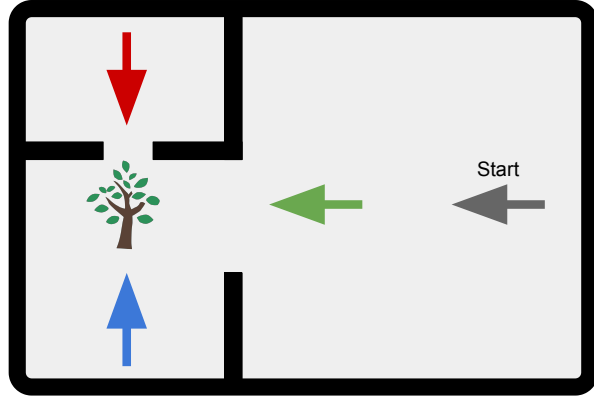


Figure 19: Example environment for approach pose planning. All approach poses are feasible; however, the red pose is not reachable from the start. The green pose is better than the blue pose since it is easier to reach.

In the second stage, the planner checks whether the feasible approach poses are attainable, i.e., can the harvester drive to them. Note that a feasible approach poses such as the red one in Fig. 19 is not necessarily attainable. The subroutine for attainability checking is summarized in Alg. 2. We build upon a standard RRT* planner that grows a random tree, as described in [Karaman and Frazzoli, 2011]. Instead of trying to connect the single goal pose (as standard RRT*) to the rest of the tree, we attempt to connect every candidate approach pose. Planning terminates when the allotted planning time runs out. The footprint used for collision checking inside Alg. 2 is shown in Fig. 17a. As a steering function inside the RRT*, we use the Reeds-Shepp (RS) curves [Reeds and Shepp, 1990] as the steering function. The turning radius parameter

was set to 8.3 m.

The rationale behind the planner’s second stage is that an attainable approach pose has a high probability of having a collision-free connection to the rest of the random tree. For example, the green pose is a better approach pose compared to the blue one in Fig. 19. The environment around the green pose is less cluttered, so the probability of a successful connection is higher. A beneficial feature of the described approach (Alg. 2) is outsourcing the final approach pose selection to the RRT*. Note that using the RRT* in its standard form would require the user to pick an approach pose, a challenging task since we do not know which ones are attainable *a priori*. Since fewer approach poses ensure faster convergence, the proposed framework allows the use of heuristics for pruning the approach pose candidate set. Pruning heuristics can be a wide array of constraints and rules, thus allowing for great flexibility (e.g., discard approach poses where heading changes more than 90°).

Algorithm 2 Path and approach pose planner

```

1: procedure COMPUTEPATHANDAPPROACHPOSES( $x_T, y_T$ )
2:    $x_T, y_T \leftarrow \text{GETNEXTTARGETLOCATION}()$ 
3:    $p_s \leftarrow \text{startingPose}$ 
4:    $rrt.\text{INITIALIZE}(p_s)$ 
5:    $\text{candidateApproachPoses} \leftarrow \text{COMPUTECANDIDATEAPPROACHPOSES}(x_T, y_T)$ 
6:   while  $t_{cpu} < T_{max}$  do
7:      $rrt.\text{GROWTREE}()$ 
8:     for each  $p_i$  in  $\text{candidateApproachPoses}$  do
9:        $rrt.\text{CONNECTTOTREE}(p_i)$ 
10:  return  $(p_i, rrt.\text{GETPATH}())$ 

```

The proposed approach pose planning takes into account almost all DoFs that HEAP has to offer. It allows the machine to turn the arm and approach trees from any angle. Furthermore, the harvester can utilize both driving directions when navigating to the goal target. One could still improve the approach pose generation to anticipate the arm turning direction. Algorithm 1 uses collision footprint shown in Fig. 17b which is clearly conservative since the arm doesn’t have to make a full 360° turn. Anticipating the turning direction would allow shrinking the collision footprint, which is very beneficial in cluttered environments such as one shown in Fig. 18. Another possible improvement is to adapt the number of approach pose candidates based on the environment. Generating too many approach pose candidates slows down the planning while marginally contributing to finding better solutions when the obstacle density is low.

8.3 Arm and Grasp Pose Planning

The grasp pose planner receives a tree position from the tree detection subsystem and computes the desired gripper orientation. Since for our demonstration, we use a gripper instead of a standard tree cutting tool (such as [Menzi Muck , 2020]), we emulate the same behavior by fixing the roll and pitch of the gripper and by computing the yaw angle such that the cabin faces the tree. The kinematic properties of HEAP and harvester machines in general with an arm that only moves in a plane allow us to come up with a simple arm planning algorithm. To reach the desired grasp pose, we design a three-stage maneuver that requires minimal space:

1. Retract the arm
2. Turn the cabin
3. Extend the arm

The approach pose planner (see Sec. 8.2.2) ensures that there is enough space for the whole arm maneuver. An exemplary arm plan is shown in Fig. 20 (stages of the maneuver are indicated with numbers). Intermediate poses (waypoints) are visualized with coordinate systems. We compute Hermite polynomials between the adjacent waypoints to form a trajectory, and we limit the average linear and angular velocity along the spline.

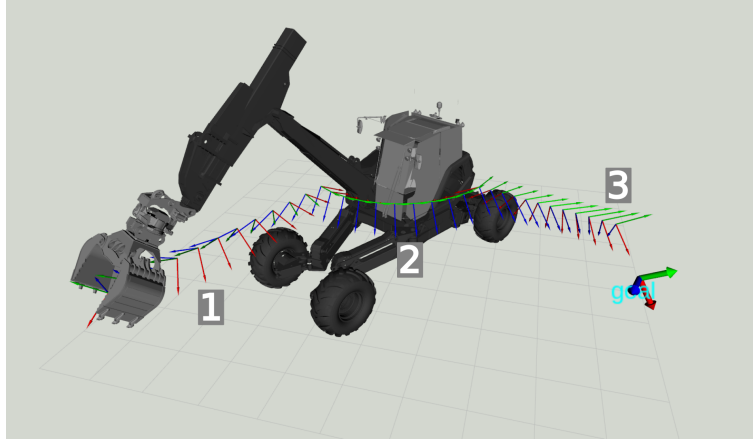


Figure 20: Plan for the arm end effector. Intermediate poses are visualized with coordinate systems. Each axis (x, y, z) corresponds to a different color (red, green, blue). A thick coordinate system and "goal" sign denote the final desired pose. Numbers correspond to different maneuver stages: 1) retract, 2) turn, 3) extend.

9 Results

The presented system components are individually tested and evaluated for complete harvesting missions in the forest and on our testing field.

9.1 Tracking

The tracking accuracy of the proposed chassis controller is evaluated on an open test field with good GPS reception to measure the tracking accuracy (Fig. 21). HEAP was commanded to follow three different paths shown in Fig. 22. The machine is denoted with a pointed polygon. Fig. 22a shows tracking a long path on inclined terrain (see Fig. 21b). A combination of inclined and wet terrain caused the HEAP to slide sideways. This can also be observed in the path visualization: the heading is not tangential to the path. The machine is pointing towards the slope to compensate for sliding to the side. The same behavior can be observed in Fig. 22b when the machine drives backward on the inclined terrain. In Fig. 22c we asked HEAP to reorient itself on the flat part of the testing field. The planned maneuver requires performing cusps and change the driving direction multiple times.

We evaluate the average deviation from the trajectory using RTK GPS as a ground truth. For the run shown in Fig. 22a the chassis controller is able to achieve mean absolute tracking error of 0.461 m over 34.1 m distance traveled and for the run shown in Fig. 22b the error was 0.684 m over distance of 44.28 m. While performing reorientation on the flat terrain, the mean absolute error was 0.222 m over distance traveled of 44.48 m (with all direction changes). One can observe that inclined terrain presents a bigger challenge for the tracking controller than direction changes. We note that the test field was fairly wet during the experiments, which negatively affected the amount of traction available. Forestry operations are typically performed when the ground is either dry or frozen, which reduces these slipping issues.

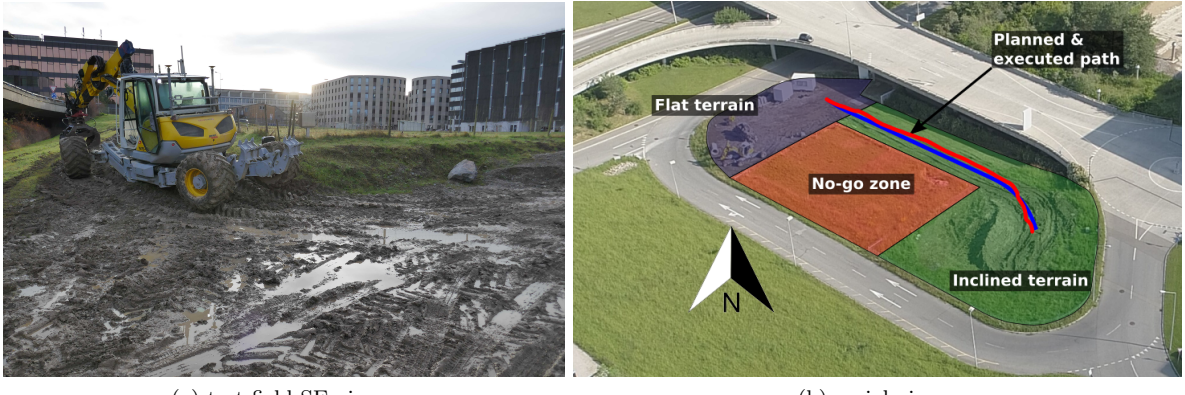


Figure 21: Photos of our testing field, not all images were taken at the same time. **Left:** View looking south-east with the machine parked. The area shown is flat. **Right:** Aerial view of the field with different classes of terrain labeled. We overlay the planned (blue) and executed (red) path from one tracking experiment (see Fig. 22a).

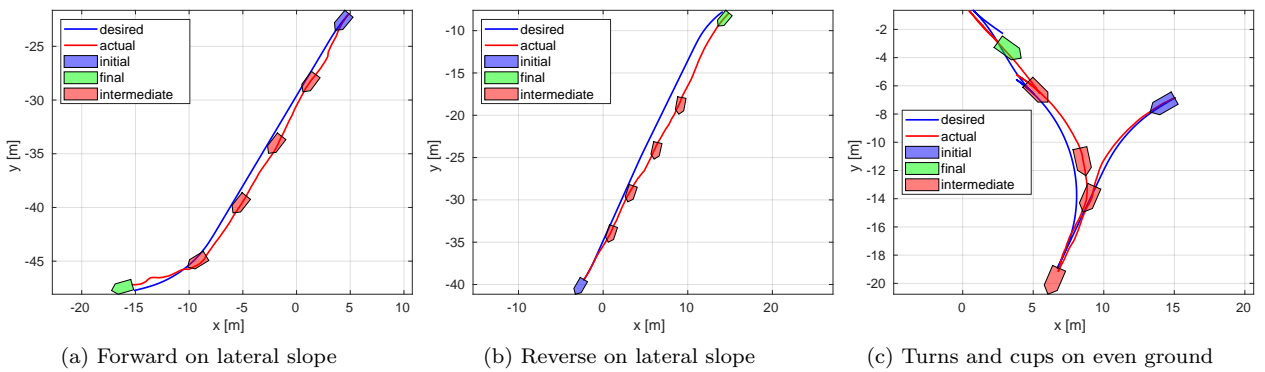


Figure 22: Experiments were conducted to determine the tracking accuracy of our chassis control approach. In blue color, the planner’s desired plan has been shown; red color denotes the actual tracked path. The initial orientation of the excavator is shown in blue color and the final one in red. The size of the vehicle is not drawn to scale.

9.2 Planning

We evaluate the approach pose planning pipeline proposed in Sec. 8.2.2 in simulated scenarios and in two experiments on different terrain: test field and forest patch. We ask the planner to compute both path and an approach pose to grab the selected target trees.

We created a simulated forest by sampling the number of trees from a Poisson distribution and their positions and radii from a uniform distribution. We consider two scenarios: in the first one, there is a forest alley that can be used for driving (see Fig. 23a). This resembles the situation encountered during the field experiments. There is no forest alley in the second scenario, and the harvester has to navigate between the trees (see Fig. 24a). Such a scenario is common when using a smaller machine such as one shown in Fig. 2a.

For the forest alley scenario, we ensure the alley at least 2.8 m wide. For comparison, the harvester path planning footprint has a width of 2.4 m and the approach pose planning footprint is 4.8 m wide at its widest point. Note that as the forest gets denser, there might not be enough space to turn the cabin, and therefore

no feasible approach poses. We choose several trees (max 50) at random within the 6 m distance from the forest alley middle (HEAP has a reach of about 8 m) to be the targets. Black dots represent trees while target trees are colored red in Fig. 23a. Each target is deemed feasible if we can find a path to it within 30 s of planning. An example path is shown in green; the starting pose and the planned approach pose are denoted with a blue and red arrow, respectively. In this particular example, the plan requires the harvester to drive forward and turn the cabin to grab the tree encircled orange. Quantitative evaluations of the planner are shown in Fig. 23, we compute the metrics only for feasible targets.

The percentage of feasible targets (see Fig. 23b) drops as the forest's density grows. However, one can see that the planner maintains a high success rate. Besides the success rate, we evaluate times required to generate candidate approach poses $t_{approach}$, time until first solution inside the RRT* planner t_{init} and we show the total planning time t_{total} (Fig. 23c). One can observe that the RRT* planner finds the first solution rather quickly (in the order of 10 ms). The most expensive part of the pipeline is the approach pose generation which in the worst case takes about 6 s. Planning times tend to shorten as the forest density increases since many approach poses can be discarded in the early stage of collision checking. In contrast, for low forest densities, almost all approach pose footprints have to be checked for collisions. For the experiments presented, the planner considers 14060 approach pose candidates in total (no pruning heuristics were applied). In this work, we use single-threaded implementation; however, the approach pose generation can be easily parallelized to decrease computation time. Lastly, we measured the distances between the starting pose and the planned approach poses (see Fig. 23d). We show the length of the first found path d_{init} and the length of the optimized path d_{final} (after running RRT* for 5 s). Lastly, the graph shows Euclidean distance between start and finish d_{lb} which is a lower bound on the path length. We can see that the planned path is close to the lower bound in all cases.

As a second scenario, we evaluated planning performance while navigating an unstructured forest. The forest was generated using the same probability distributions as in the scenario above. We leave a clear area (10 m by 10 m) in the middle of the map to ensure a feasible starting pose. The target trees were selected at random with a maximum of 50 trees. Again, we check the feasibility for each target by running the planner for 30 s.

Performance measures shown in Fig. 24b - Fig. 24d are calculated only for feasible targets. One can observe a much faster drop in the percent of feasible targets (compared to the forest alley scenario). In most cases, our planner finds the solution rather quickly (600 ms in the worst case). We can also notice that the success rate drops compared to the previous scenario since there is no forest alley. The planner has to find a path through narrow passages, a hard case for sampling-based planners. The success rate for densities between 0.05 and 0.15 can be increased with longer planning times. For forest densities higher than 0.1 the HEAP harvester simply does not fit between the trees. Hence the set of feasible targets comprises the trees around the clear patch in the middle of the simulated forest. In this case, the success rate goes again to 100 %.

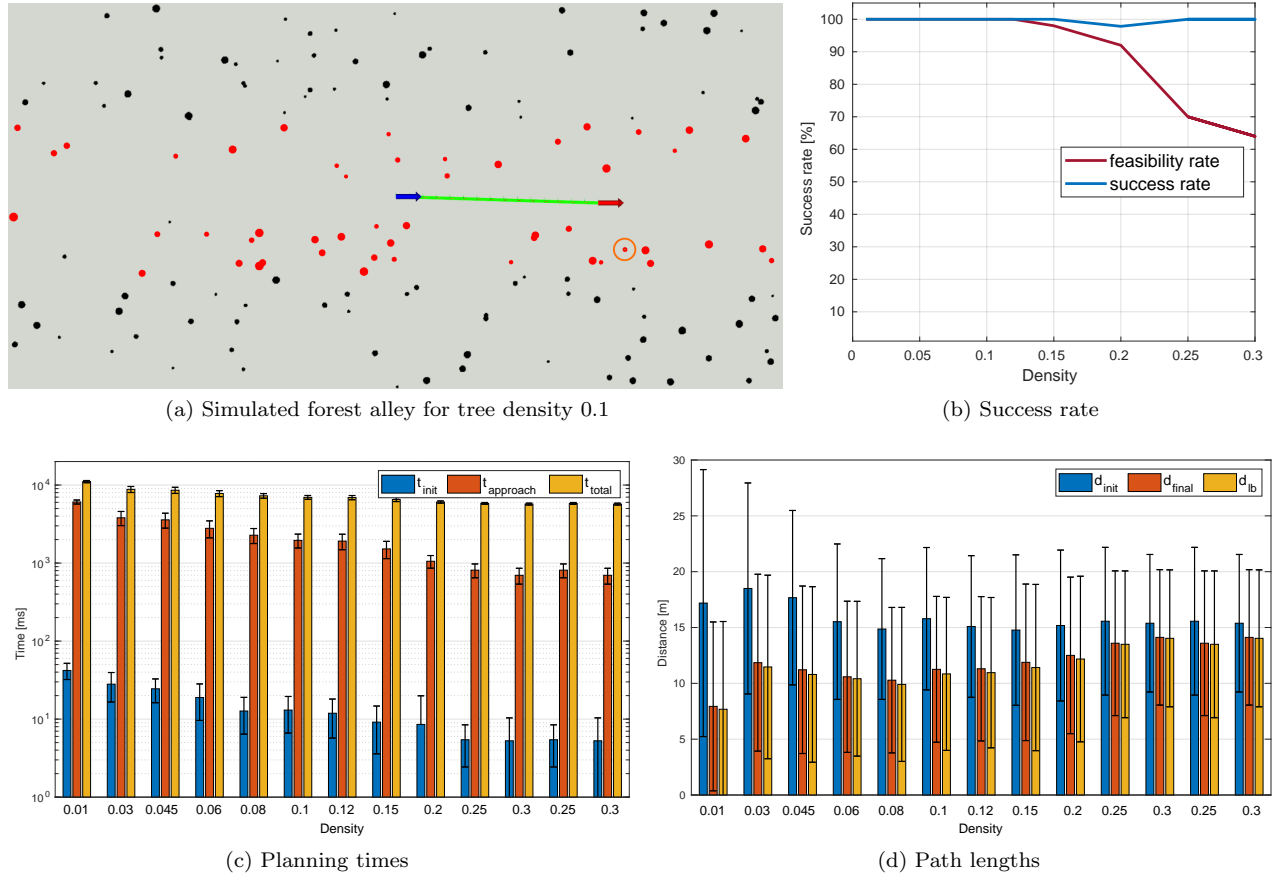


Figure 23: Joint path and approach pose planning for the forest alley scenario. **Top Left:** Top view of the random forest with the path and approach pose planned. The harvester starts from the blue arrow to grab the tree encircled orange. Path is shown in green and the final approach pose in red. Black dots represent the trees and red dots are the remaining target trees. **Top Right:** Percentage of feasible targets and the success rate as the forest density increases. Success rate is calculated as number of successful planning attempts divided by the number of feasible targets. **Bottom Left:** Planning times against varying forest density, note the logarithmic scale on the y axis **Bottom Right:** Path lengths as a function of varying forest density.

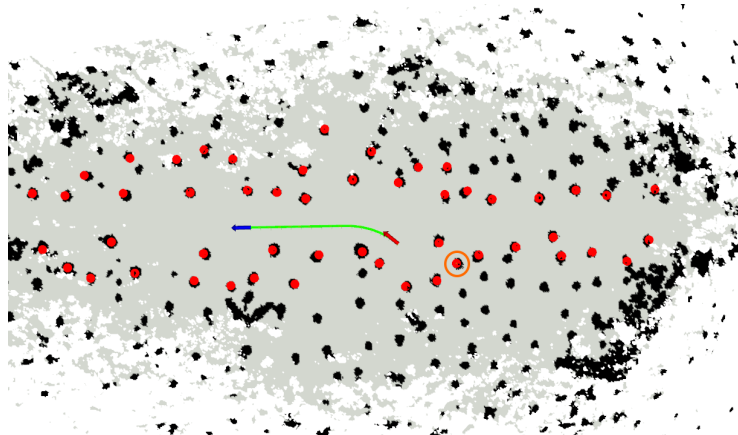
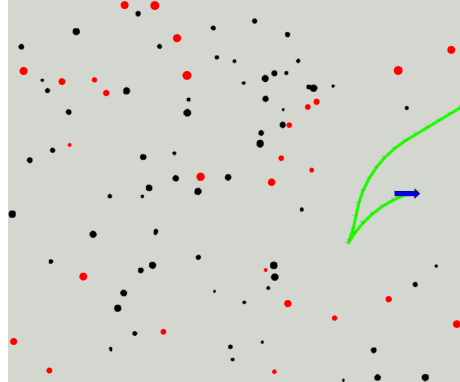


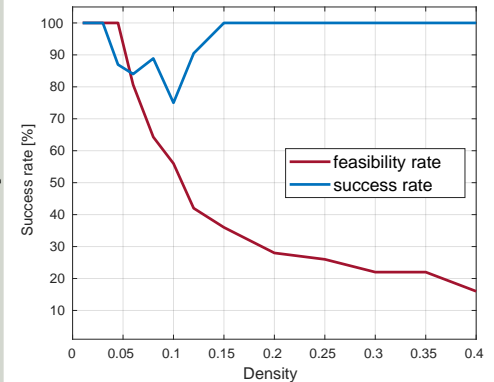
Figure 25: Obstacle map for the forest patch scenario. Obstacles are shown in black color whereas free space is shown in gray color. The targets are denoted with red cylinders.

Table 3: Planning statistics for the forest patch scenario.

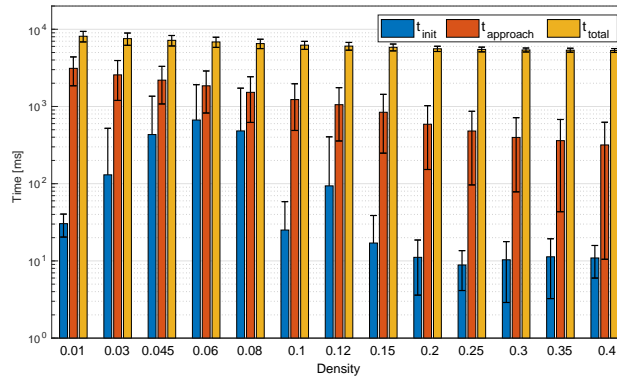
num targets	51
success rate	0.96
time until first solution [ms]	(11.11 ± 8.33)
approach pose generation time [ms]	(1142 ± 378)
total planning time [s]	(5.0 ± 0.12)
initial path length [m]	(16.70 ± 9.89)
optimized path length [m]	(14.98 ± 10.65)
length lower bound [m]	(14.67 ± 10.96)



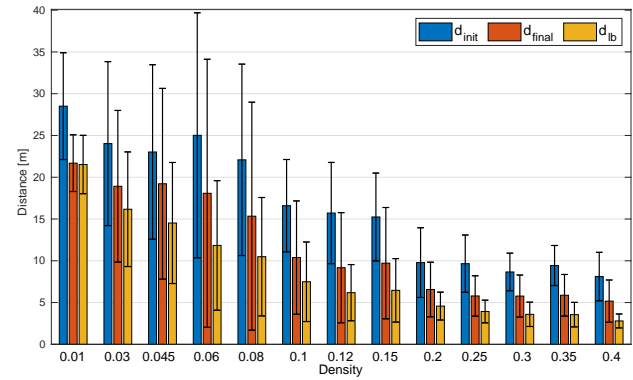
(a) Simulated unstructured forest for tree density 0.1



(b) Success rate



(c) Planning times



(d) Path lengths

Figure 24: Joint path and approach pose planning for the unstructured forest scenario. **Top Left:** Top view of the random forest with the path and approach pose planned. See Fig. 23 for explanations of the colors in the image. **Top Right:** Success rate as the forest density increases. **Bottom Left:** Planning times against varying forest density, note the logarithmic scale on the *y* axis **Bottom Right:** Path lengths as a function of varying forest density.

To evaluate the planning performance under realistic conditions, we took a map of our testing field and the forest patch where we conducted the tests. The forest patch map with target trees is shown in Fig. 25. Black dots represent trees and other obstacles, while target trees are denoted with red dots. We manually selected the trees along the forest alley, discarding any tree without path computed within 60s of planning. The forest density at the testing site was estimated to be about 0.07 (trees/m²). The planner achieved a success rate of about 96 % which is comparable to the simulated scenario (100 %). Furthermore, the time t_{init} is comparable to the one in the simulated scenario. $t_{approach}$ is lower than simulated, most likely since the actual forest alley width is smaller than the simulated one. On the testing field, the planner achieved the success rate of 100 %.

9.3 Tree Detection

We evaluated tree detection offline by mimicking local maps assembled from harvester sensors during the scanning maneuver. We select 6 m by 6 m patches inside the map shown in Fig. 8a and ask the tree detector to detect all trees inside the cropped map. The patch size roughly corresponds to the area covered by vertical Velodyne sensor frustum after the scanning maneuver. The detection procedure discarded clusters with diameter bigger than 2.5 m, fewer than 1000 points or with gravity alignment score less than 0.8 (as defined in Sec. 6); the result is shown in Fig. 26. One can observe successful tree detections even in the

presence of vegetation. Heavy clutter in the scene, such as in patch five and patch 12, causes the detector to reject segmented tree clusters, incorrectly producing false negatives. In case no trees are detected close to the target, the harvester resorts to blind grabbing at the target location (known *a priori* from the map).

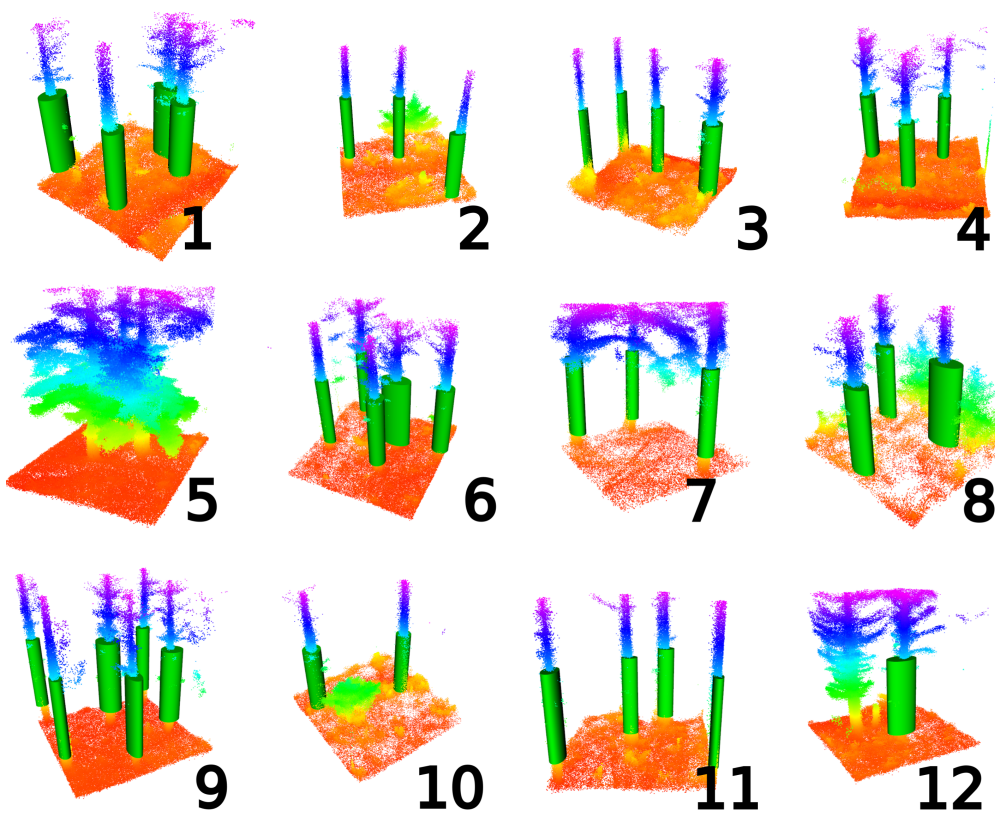
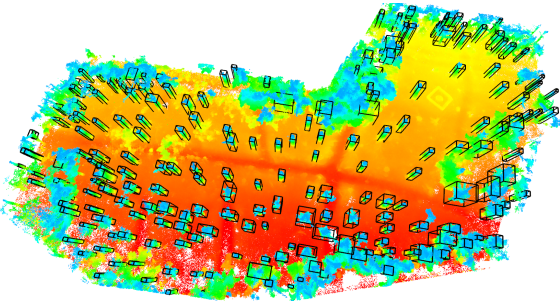


Figure 26: 6 m by 6 m point cloud patches from the testing site. Red corresponds to the lowest and purple to the highest elevation. Tree detections are shown with green cylinders.

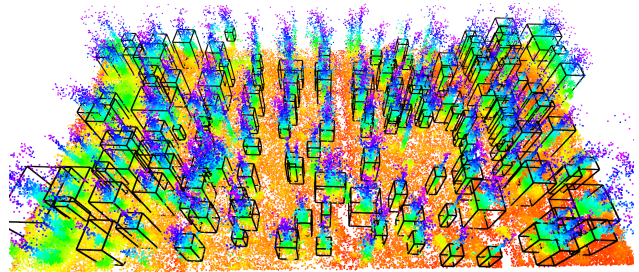
9.3.1 Tree Detector for Mission Planning

In this section, we present the use of a tree detector as a mission planner. The tree detector can be used to extract tree coordinates for clear-cutting missions or as a mission planning aid. We ran the tree detection offline on three forest patches of different styles, all shown in the figures below. The ground plane was filtered out, and the procedure presented in Sec. 6 was used. We manually identify the trees in each point cloud to obtain the actual number of trees.

Fig. 27a shows the first forest patch together with tree detections. The patch has about 246 (both evergreen and deciduous) trees, and the tree detector correctly detected 210 of them. There were 14 false positives, and 36 trees were not detected (false negatives), which amounts to a precision of 94 % and recall rate of about 85 %. The point cloud of the second forest patch and detected trees are shown in Fig. 27b. In total, there are 163 (spruce) trees, and the tree detector correctly detected 143 of them. There were six false positives, and 20 trees were not detected, which amounts to a precision of 96 % and recall rate of about 88 %. The last forest patch is shown Fig. 28. The Forest patch has about 285 trees (all deciduous trees). The tree detector detected in total 266 trees. Four detections were false positives, whereas the number of false negatives was 19. These numbers give the tree detector precision of 98 % and recall rate of 93 %.



(a) Mixed forest with detected trees



(b) Spruce forest with detected trees

Figure 27: Maps and tree detections for two forest patches. Detected trees are denoted with black bounding boxes. Red/yellow color corresponds to the lowest elevation and blue/purple to the highest. **Left:** Forest with both evergreen and deciduous trees. Note the heavy clutter towards the edges of the map. **Right:** Forest with mainly spruce trees.

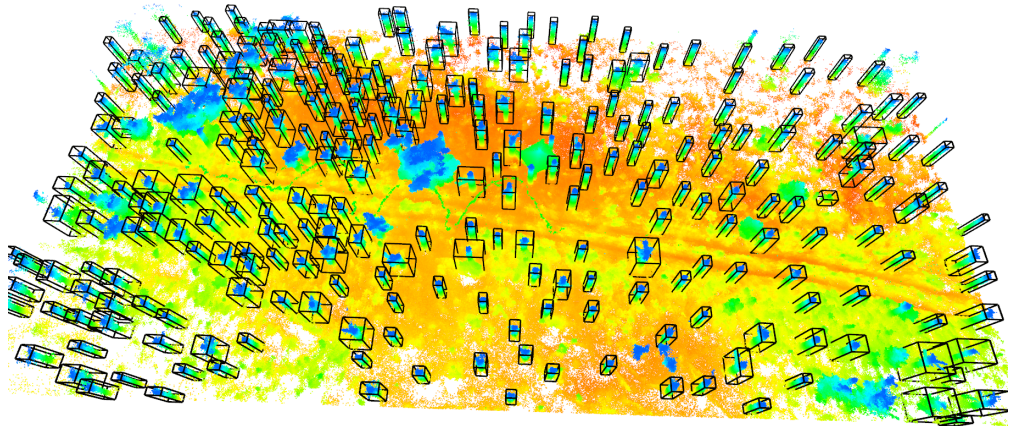


Figure 28: Forest patch and detected trees denoted with black bounding boxes. The forest patch consists of deciduous trees.

9.4 Localization

We evaluated the localization of the proposed sensor module running Google Cartographer SLAM in three different terrains: two forest patches and our testing field. We collect the dataset with the sensor module presented in 3.2, and we run the SLAM offline, which produces a consistent, optimized map. Subsequently, we set the Cartographer in the localization mode and tune it such that both the LIDAR odometry and loop closures run in real-time. Note that Cartographer running in the localization mode does not try to build a global map (see [Hess, 2017]). We are interested in quantifying performance degradation when running in real-time localization mode without joint map and trajectory bundle adjustment. We localize in a previously built map and compare the localized pose against the bundle adjusted trajectory (pseudo-ground-truth). Paths overlaid inside the map can be seen in Fig. 29 while the top view plots of the trajectories can be seen in Fig. 30.

We evaluate the localization error as the euclidean distance between the corresponding points on the localized trajectory and pseudo ground-truth trajectory. For the test field, we obtain a translational error of 0.11 ± 0.09 meters; the trajectory length was 255.8 m. Trajectory length for the first forest dataset was 158.37 m, and Cartographer localizes with the error of 0.17 ± 0.28 meters. Inside, the second forest trajectory was

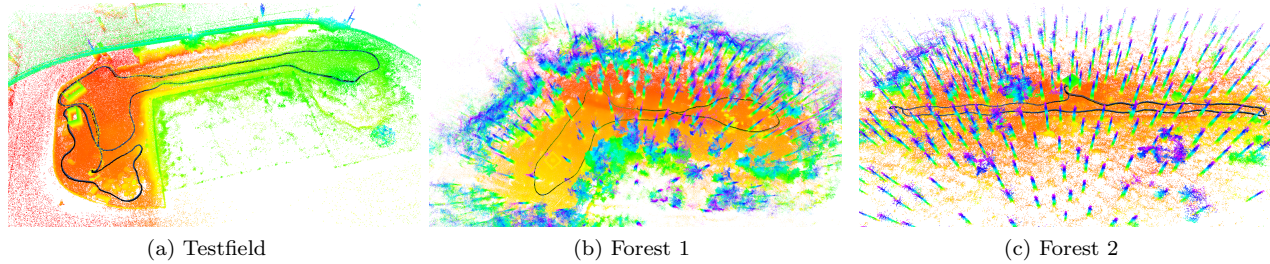


Figure 29: The trajectories from the localization field experiments overlaid with the map.

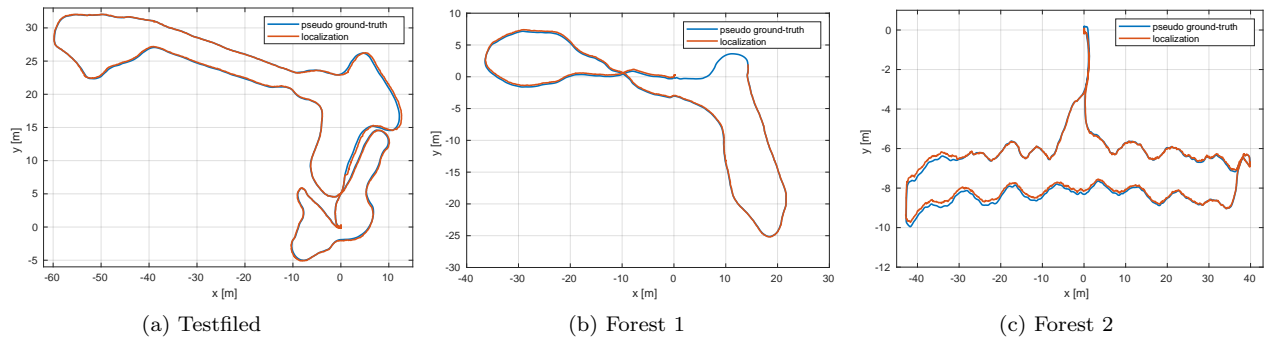


Figure 30: The trajectories from the localization field experiments viewed from above. Forest 1 and Forest 2 are datasets from two different forests.

183.27 meters long, and the localization error was 0.25 ± 0.28 meters.

9.5 Fully integrated system

This section presents snapshots of a fully integrated system performing a harvesting mission. We tested our system on a test field where HEAP was commanded to grab "tree trunks". One tree trunk is composed of three wooden logs strapped together such that they can stand straight up. In addition to our test field, we have performed the second set of experiments in a small forest alley in a real forest with fully grown adult trees. We show snapshots of 1 operational cycle between grasping two trees Fig. 31. The reader is encouraged to watch a video accompanying this submission since it offers a better insight⁵.

It takes about 1-2.5 minutes for the machine to complete the entire cycle, depending on how far the cabin has to turn and how far it has to drive. The cabin turns and driving are pretty conservative (slow), and the time could be improved drastically by speeding them up. The proposed system was able to run without any changes in both the test field and the forest. Furthermore, we were able to successfully detect both tree trunks and wooden logs and perform a grab. A human operator was often inside the cabin for safety.

10 Conclusions & Discussion

We present a first attempt at performing automated forestry operations using a full-sized harvester to the best of our knowledge. The approach presented is targeted for precision harvesting. We design a lightweight and versatile sensor module that can be used for mapping and later mounted on the harvester for localization.

⁵<https://youtu.be/n11d2qw6dD0>

Using the sensor module and SLAM system enables the HEAP harvester to navigate under the forest canopy without relying on GPS signal. Our system can plan approach poses in confined spaces, and it can negotiate challenging terrain by combining chassis balancing controller with the path following controller. In this work, we rely on a human expert to specify target trees for harvesting. To combat the localization error and enable precision harvesting, we plan grasping poses in the local frame using a geometric detection algorithm operating on the point cloud assembled from the laser sensor. Lastly, parts of our planning and mapping software stack have been made open source for the community.

Each of the modules (e.g., planning, mapping) has been first tested and benchmarked individually before integrating them into a complete precision harvesting mission. For example, we first tested planning and control with RTK GPS before adding the SLAM system. Stepwise integration was essential to isolate problems.

Experimental verification of our approach during the wet season was unfortunate, and the biggest problem occurring was that the machine would get stuck in the mud from time to time. This problem was somewhat mitigated by using chains and putting wooden logs and branches in the mud to improve traction. We do not see this as a limitation of our system since forestry operations typically find a place during dry seasons.

We point out that pure geometry-based localization (or detection) can exhibit failures in the forest. For example, a crowd of humans observing the machine can look very similar to tree trunks in a point cloud, which on one occasion caused the SLAM to produce spurious pose estimates. Furthermore, we had a few cases of sun rays directly shining on our camera, which caused the visual odometry to diverge. Subsequently, the whole state estimation pipeline diverged despite the pure LIDAR odometry working well. This seeks an approach that can adequately detect sensor degeneration to ensure robust mapping and localization in all cases.

Future improvements will focus on adding more sensors and implementing health checking systems to mitigate state estimation problems. For example, one could run visual and LIDAR based SLAM to increase robustness since these two kinds of sensors are complementary to each other (similar as in [Khattak et al., 2020]). We will also improve the approach pose planner by incorporating the footprint adaptation and adjusting the number of generated approach poses based on the environment, as noted in Section 8. Furthermore it would be interesting to benchmark different planners (e.g. Probabilistic Roadmap (PRM) or hybrid A* algorithm [Dolgov et al., 2010]). Incorporating the improvements outlined above will bring us one step closer to fully automated precision forestry that will increase yields and relieve humans from tedious labor.



Figure 31: Snapshots of an operational cycle between grabbing two trees. HEAP re-positioning the base close to the tree (snapshots 1-6) followed by scanning the environment and building a local map (snapshots 7-9). Finally, HEAP grabs the tree by extending the arm (snapshots 10-12) and retracting it (snapshots 13-15). After retracting the arm, the harvester is ready to grab the next tree and whole cycle repeats.

References

Babin, P., Dandurand, P., Kubelka, V., Giguère, P., and Pomerleau, F. (2019). Large-scale 3d mapping of sub-arctic forests. *arXiv preprint arXiv:1904.07814*.

Bellicoso, C. D., Gehring, C., Hwangbo, J., Fankhauser, P., and Hutter, M. (2016). Perception-less terrain adaptation through whole body control and hierarchical optimization. In *2016 IEEE-RAS 16th International Conference on Humanoid Robots (Humanoids)*, pages 558–564. IEEE.

Carius, J., Wermelinger, M., Rajasekaran, B., Holtmann, K., and Hutter, M. (2018). Deployment of an autonomous mobile manipulator at mbzirc. *Journal of Field Robotics*, 35(8):1342–1357.

Choudhry, H. and O’Kelly, G. (2018). Precision forestry: A revolution in the woods. Retrieved November 27 2019 from <https://www.mckinsey.com/industries/paper-forest-products-and-packaging/our-insights/precision-forestry-a-revolution-in-the-woods>.

Dolgov, D., Thrun, S., Montemerlo, M., and Diebel, J. (2010). Path planning for autonomous vehicles in unknown semi-structured environments. *The international journal of robotics research*, 29(5):485–501.

Eidson, J. C. (2006). *Measurement, control, and communication using IEEE 1588*. Springer Science & Business Media.

Fankhauser, P., Bloesch, M., and Hutter, M. (2018). Probabilistic terrain mapping for mobile robots with uncertain localization. *IEEE Robotics and Automation Letters (RA-L)*, 3(4):3019–3026.

Fankhauser, P. and Hutter, M. (2016). A universal grid map library: Implementation and use case for rough terrain navigation. In *Robot Operating System (ROS)*, pages 99–120. Springer.

Forestry Focus (2018). Thinning. Retrieved November 26 2019 from <https://www.forestryfocus.ie/growing-forests-3/establishing-forests/thinning/>.

Gawel, A., Blum, H., Pankert, J., Krämer, K., Bartolomei, L., Ercan, S., Farshidian, F., Chli, M., Gramazio, F., Siegwart, R., et al. (2019). A fully-integrated sensing and control system for high-accuracy mobile robotic building construction. *arXiv preprint arXiv:1912.01870*.

Georgsson, F., Hellström, T., Johansson, T., Prorok, K., Ringdahl, O., and Sandström, U. (2005). *Development of an Autonomous Path Tracking Forest Machine: a status report*.

Giftthaler, M., Farshidian, F., Sandy, T., Stadelmann, L., and Buchli, J. (2017). Efficient kinematic planning for mobile manipulators with non-holonomic constraints using optimal control. In *2017 IEEE International Conference on Robotics and Automation (ICRA)*, pages 3411–3417. IEEE.

Harrison, A. and Newman, P. (2011). Ticsync: Knowing when things happened. In *2011 IEEE International Conference on Robotics and Automation*, pages 356–363. IEEE.

Hawkinson, D. (2017). Forestry industry. Retrieved January 22 2021 from <https://forestreresources.org/resources/woods-to-mill/item/870-addressing-the-labor-shortage-in-the-forestry-industry>.

Hellström, T., Lärkeryd, P., Nordfjell, T., and Ringdahl, O. (2008). Autonomous forest machines: Past present and future.

Hess, W. (2017). Cartographer online documentation. Retrieved December 06 2019 from <https://google-cartographer.readthedocs.io/en/latest/#>.

Hess, W., Kohler, D., Rapp, H., and Andor, D. (2016). Real-time loop closure in 2d lidar slam. In *2016 IEEE International Conference on Robotics and Automation (ICRA)*, pages 1271–1278. IEEE.

Holopainen, M., Västaranta, M., and Hyppä, J. (2014). Outlook for the next generation’s precision forestry in finland. *Forests*, 5(7):1682–1694.

Hutter, M., Leemann, P., Hottiger, G., Figi, R., Tagmann, S., Rey, G., and Small, G. (2016). Force control for active chassis balancing. *IEEE/ASME Transactions on Mechatronics*, 22(2):613–622.

Hutter, M., Leemann, P., Stevsic, S., Michel, A., Jud, D., Hoepflinger, M., Siegwart, R., Figi, R., Caduff, C., Loher, M., et al. (2015). Towards optimal force distribution for walking excavators. In *2015 international conference on advanced robotics (ICAR)*, pages 295–301. IEEE.

Hyyti, H., Lehtola, V. V., and Visala, A. (2018). Forestry crane posture estimation with a two-dimensional laser scanner. *Journal of Field Robotics*, 35(7):1025–1049.

Johns, R. L., Wermelinger, M., Mascaro, R., Jud, D., Gramazio, F., Kohler, M., Chli, M., and Hutter, M. (2020). Autonomous dry stone. *Construction Robotics*, 4(3):127–140.

Jud, D. (2018). Heap. Retrieved November 27 2019 from <https://rsl.ethz.ch/robots-media/heap.html>.

Jud, D., Leemann, P., Kerscher, S., and Hutter, M. (2019). Autonomous free-form trenching using a walking excavator. *IEEE Robotics and Automation Letters*, 4(4):3208–3215.

Kalmari, J., Backman, J., and Visala, A. (2014). Nonlinear model predictive control of hydraulic forestry crane with automatic sway damping. *Computers and Electronics in Agriculture*, 109:36–45.

Karaman, S. and Frazzoli, E. (2011). Sampling-based algorithms for optimal motion planning. *The international journal of robotics research*, 30(7):846–894.

Khattak, S., Nguyen, H., Mascarich, F., Dang, T., and Alexis, K. (2020). Complementary multi-modal sensor fusion for resilient robot pose estimation in subterranean environments. In *2020 International Conference on Unmanned Aircraft Systems (ICUAS)*, pages 1024–1029. IEEE.

Kim, S., Jang, K., Park, S., Lee, Y., Lee, S. Y., and Park, J. (2019). Whole-body control of non-holonomic mobile manipulator based on hierarchical quadratic programming and continuous task transition. In *2019 IEEE 4th International Conference on Advanced Robotics and Mechatronics (ICARM)*, pages 414–419. IEEE.

Komatsu Corporation (2019). Harvesters - product catalogue. Retrieved November 26 2019 from <https://www.komatsuforest.com/forest-machines/our-wheeled-harvesters>.

Kuwata, Y., Teo, J., Karaman, S., Fiore, G., Frazzoli, E., and How, J. (2008). Motion planning in complex environments using closed-loop prediction. In *AIAA Guidance, Navigation and Control Conference and Exhibit*, page 7166.

La Hera, P. M., Mettin, U., Westerberg, S., and Shiriaev, A. S. (2009). Modeling and control of hydraulic rotary actuators used in forestry cranes. In *2009 IEEE International Conference on Robotics and Automation*, pages 1315–1320. IEEE.

Lindroos, O., Ringdahl, O., La Hera, P., Hohnloser, P., and Hellström, T. H. (2015). Estimating the position of the harvester head—a key step towards the precision forestry of the future? *Croatian Journal of Forest Engineering: Journal for Theory and Application of Forestry Engineering*, 36(2):147–164.

Menzi Muck (2020). Menzi muck construction equipment accessories. Retrieved March 30 2021 from <https://www.menzimuck.com/en/product-groups/menzi-construction-equipment-accessories/>.

Miettinen, M., Ohman, M., Visala, A., and Forsman, P. (2007). Simultaneous localization and mapping for forest harvesters. In *Proceedings 2007 IEEE International Conference on Robotics and Automation*, pages 517–522. IEEE.

Mikhaylov, M. and Lositskii, I. (2018). Control and navigation of forest robot. In *2018 25th Saint Petersburg International Conference on Integrated Navigation Systems (ICINS)*, pages 1–2. IEEE.

Morales, D. O., Westerberg, S., La Hera, P., Mettin, U., Freidovich, L. B., and Shiriaev, A. S. (2011). Open-loop control experiments on driver assistance for crane forestry machines. In *2011 IEEE International Conference on Robotics and Automation*, pages 1797–1802. IEEE.

Morita, M., Nishida, T., Arita, Y., Shige-eda, M., di Maria, E., Gallone, R., and Giannoccaro, N. I. (2018). Development of robot for 3d measurement of forest environment. *Journal of Robotics and Mechatronics*, 30(1):145–154.

Naesset, E. (1997). Determination of mean tree height of forest stands using airborne laser scanner data. *ISPRS Journal of Photogrammetry and Remote Sensing*, 52(2):49–56.

Ortiz Morales, D., Westerberg, S., La Hera, P. X., Mettin, U., Freidovich, L., and Shiriaev, A. S. (2014). Increasing the level of automation in the forestry logging process with crane trajectory planning and control. *Journal of Field Robotics*, 31(3):343–363.

Parker, R., Bayne, K., and Clinton, P. W. (2016). Robotics in forestry. *NZ Journal of Forestry*, 60(4):9.

Reeds, J. and Shepp, L. (1990). Optimal paths for a car that goes both forwards and backwards. *Pacific journal of mathematics*, 145(2):367–393.

Renner, M., Sweeney, S., and Kubit, J. (2008). *Green Jobs: Towards decent work in a sustainable, low-carbon world*. UNEP.

Roßmann, J., Krahwinkler, P., and Bücken, A. (2009). Mapping and navigation of mobile robots in natural environments. In *Advances in Robotics Research*, pages 43–52. Springer.

Rossmann, J., Krahwinkler, P., and Schlette, C. (2010). Navigation of mobile robots in natural environments: Using sensor fusion in forestry. *J. Syst. Cybern. Inform*, 8(3):67–71.

Rossmann, J., Schluse, M., Schlette, C., Buecken, A., Krahwinkler, P., and Emde, M. (2009). Realization of a highly accurate mobile robot system for multi purpose precision forestry applications. In *2009 International Conference on Advanced Robotics*, pages 1–6. IEEE.

Rusu, R. B. (2010). Semantic 3d object maps for everyday manipulation in human living environments. *KI-Künstliche Intelligenz*, 24(4):345–348.

Rusu, R. B. and Cousins, S. (2011). 3d is here: Point cloud library (pcl). In *2011 IEEE international conference on robotics and automation*, pages 1–4. IEEE.

Schwarz, M., Rodehutskors, T., Droeischel, D., Beul, M., Schreiber, M., Araslanov, N., Ivanov, I., Lenz, C., Razlaw, J., Schüller, S., et al. (2017). Nimbro rescue: Solving disaster-response tasks with the mobile manipulation robot momaro. *Journal of Field Robotics*, 34(2):400–425.

Siciliano, B., Sciavicco, L., Villani, L., and Oriolo, G. (2010). *Robotics: modelling, planning and control*. Springer Science & Business Media.

Silvere (2017). We know your trees. Retrieved November 27 2019 from <https://silvere.com/english>.

Sucan, I. A., Moll, M., and Kavraki, L. E. (2012). The open motion planning library. *IEEE Robotics & Automation Magazine*, 19(4):72–82.

Swedish Forest Agency (2014). Swedish statistical yearbooks of forestry. Retrieved November 26 2019 from <http://klimatetochskogen.nu/en/information-sources/reports/161-sks2014-forestry-yearbook-2014/>.

Tominaga, A., Eiji, H., and Mowshowitz, A. (2018). Development of navigation system in field robot for forest management. In *2018 Joint 10th International Conference on Soft Computing and Intelligent Systems (SCIS) and 19th International Symposium on Advanced Intelligent Systems (ISIS)*, pages 1142–1147. IEEE.

Tsubouchi, T., Asano, A., Mochizuki, T., Kondou, S., Shiozawa, K., Matsumoto, M., Tomimura, S., Nakanishi, S., Mochizuki, A., Chiba, Y., et al. (2014). Forest 3d mapping and tree sizes measurement for forest management based on sensing technology for mobile robots. In *Field and Service Robotics*, pages 357–368. Springer.

United Nations Food and Agricultural Organization (2018). 2018 the state of the world's forests. Retrieved November 26 2019 from <http://www.fao.org/state-of-forests/en/>.

Von Carlowitz, H. C. and von Rohr, J. B. (1732). *Sylvicultura oeconomica*.

Wermelinger, M., Fankhauser, P., Diethelm, R., Krüsi, P., Siegwart, R., and Hutter, M. (2016). Navigation planning for legged robots in challenging terrain. In *2016 IEEE/RSJ International Conference on Intelligent Robots and Systems (IROS)*, pages 1184–1189. IEEE.

Westerberg, S. (2014). *Semi-automating forestry machines: Motion planning, system integration, and human-machine interaction*. PhD thesis, Umeå Universitet.

Yue, Y., Yang, C., Senarathne, P., Zhang, J., Wen, M., and Wang, D. (2018). Online collaborative 3d mapping in forest environment. *Forest*, 2(1.2710):4–0915.

Zhang, C., Yong, L., Chen, Y., Zhang, S., Ge, L., Wang, S., and Li, W. (2019). A rubber-tapping robot forest navigation and information collection system based on 2d lidar and a gyroscope. *Sensors*, 19(9):2136.

Zhang, J. and Singh, S. (2014). Loam: Lidar odometry and mapping in real-time. In *Robotics: Science and Systems*, volume 2, page 9.

Zhang, J. and Singh, S. (2015). Visual-lidar odometry and mapping: Low-drift, robust, and fast. In *2015 IEEE International Conference on Robotics and Automation (ICRA)*, pages 2174–2181. IEEE.

Zucker, M., Ratliff, N., Dragan, A. D., Pivtoraiko, M., Klingensmith, M., Dellin, C. M., Bagnell, J. A., and Srinivasa, S. S. (2013). Chomp: Covariant hamiltonian optimization for motion planning. *The International Journal of Robotics Research*, 32(9-10):1164–1193.